Elastic Scattering and Single-Pion Production in K^-p Interactions at 5.5 GeV/c *†

R. Engelmann, B. Musgrave, F. Schweingruber, and H. Yuta
Argonne National Laboratory, Argonne, Illinois 60439

and

B. Forman, N. Gelfand, and H. Schulz
Enrico Fermi Institute, University of Chicago, Chicago, Illinois 60637
(Received 6 December 1971)

We present results of an analysis of two-prong events for elastic scattering and single-pion production in K^-p interactions at 5.5 GeV/c. The resonance parameters for the charged and neutral $K^*(890)$ and $K^*(1420)$ are determined and the observed production and decay properties of the charged and neutral $K^*(890)$ are compared with the theoretical predictions of an absorptive one-particle-exchange model and a Regge model. The $K^*(1420)$ differential cross section and density-matrix elements are presented and the question of whether more than one resonance exists in this mass range is considered. A search for resonance effects at $K\pi$ mass beyond 1500 MeV is made. In particular, the recently reported state at 1800 MeV is discussed. A B_5-model analysis of the reaction $K^-p \to \bar{K}^0\pi^-p$ is also presented.

I. INTRODUCTION

We have analyzed data obtained from the measurement of two-prong and two-prong-plus-V^0 events for the study of elastic scattering and single-pion production in K^-p interactions at 5.5 GeV. The reactions studied are

$$K^-p \to K^-p \quad (1.1)$$
$$\to pK^-\pi^0 \quad (1.2)$$
$$\to p\pi^-\bar{K}^0 \quad (1.3)$$
$$\to K^-\pi^+n \quad (1.4)$$
$$\to \Lambda^0(\Sigma^0)\pi^+\pi^-, \quad (1.5)$$

with emphasis on reactions (1.1)–(1.4). Reaction (1.5) is included only for evaluating the background problem to reaction (1.4).

The experiment was carried out by exposing the ANL 30-in. hydrogen bubble chamber to an electrostatically separated beam of K^- mesons produced at the ZGS (zero-gradient synchrotron). The beam contamination of π^- and μ^- was estimated to be about 5% when the beam was tuned for 5.5 GeV/c.[1]

The data presented here consist of two parts. The first part (sample I) comes from manual measurements of 17 000 two-prong-plus-V^0 events and 6000 two-prong events, which yield 755 and 465 acceptable events for reactions (1.3) and (1.4), respectively. Results from this analysis have already been published.[1,2] The new data, 42 000 events, represent a continuation of the previous work using POLLY II[3] to complete all two-prong measurements (sample II).

In this paper, we include a consideration of the data reduction of the two-prong measurements to obtain samples of reactions (1.1)–(1.4), and we deal with the general features of the quasi-two-body system, in particular, production and decay of the $K^*(890)$ and the $K^*(1420)$. We stress here that data for reactions (1.2)–(1.4) in sample II are obtained from two-prong events without V^0 measurements, where particular caution is required for the event classification.

II. EXPERIMENTAL DETAILS

The experimental details for the first sample of events have been fully described,[1] and here we discuss scanning, measuring, and event identification for the second sample of events obtained from POLLY measurements. We have used the standard ANL program chain TVGP-GRIND-SUMX for the reduction of sample II. Sample II provides the major part of all data and shows essentially the same general features as observed for sample I. The results presented here represent the combined samples.

A. Scanning and Measuring

Sample II is comprised of both two-prong and two-prong-plus-V^0 events measured as two-prong events. There is then substantial overlap with the two-prong-plus-V^0 events in sample I, a higher constraint class, where most events are identified unambiguously. This sample of overlapping events provides a powerful check on background effects in the event classification for sample II.

The scanning criteria excluded from measure-

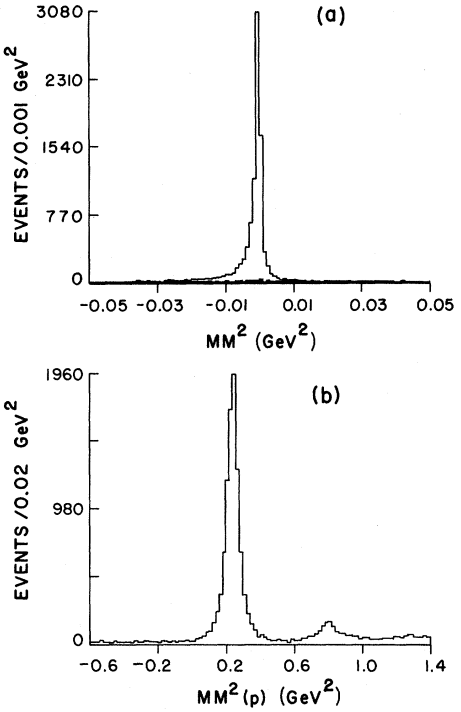

FIG. 1. (a) Missing-mass-squared (MM^2) distributions for all two-prong events. The shaded area corresponds to the events with $0 < MM^2(p) < 0.5$ GeV^2. (b) Missing-mass-squared [$MM^2(p)$] distributions for all two-prong events.

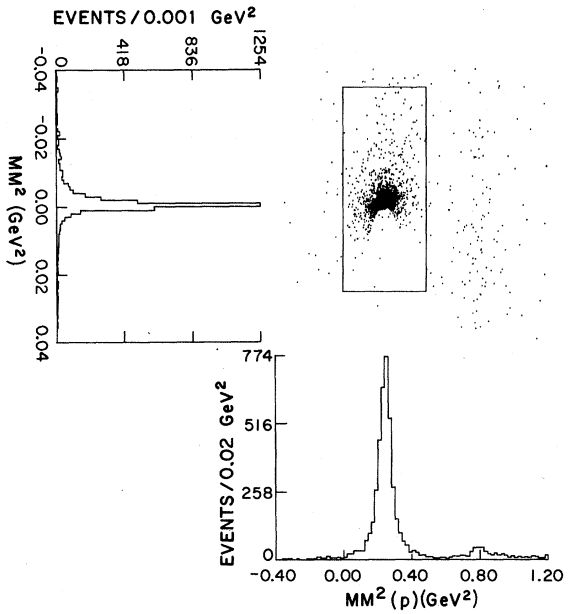

FIG. 2. Scatter plot of MM^2 vs $MM^2(p)$ for a sample of events. Events inside the rectangular box are attributed to elastic scattering.

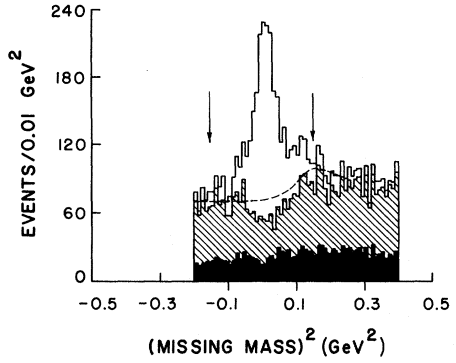

FIG. 3. Missing-mass-squared distribution for hypothesis (1.2), $K^-p \to K^-p$(MM), for all two-prong events with $-0.2 < MM^2 < 0.4$ GeV^2. For Figs. 3–6, the shaded area corresponds to the events not satisfying criterion (a) and the cross-hatched area corresponds to the events not satisfying criterion (b). The dashed curves in Figs. 3–5 show the background levels assumed and the arrows indicate the missing-mass range used for the calculation of the cross section.

ment only those events where the separation between the beam track and neighboring beam tracks was smaller than 200 μ on film. This unbiased rejection, made to facilitate event measurement on POLLY, removed about 15% of all two-prong events. We stress that this rejection did not affect the ratio of events assigned to the various channels available in the K^-p interaction. Guidance on POLLY was minimal and only involved the location of the event vertex to 1000 μ on film in the first view to be measured.

A significant advantage in using automatic measuring devices such as POLLY lies in the reliable estimates of bubble density obtained as the tracks are digitized.[3] This ionization information, together with the χ^2 probability of kinematical fit in GRIND, has been used in deciding the event classification.

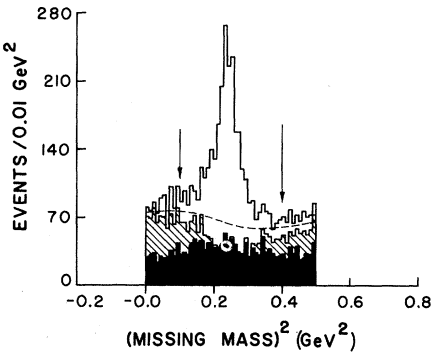

FIG. 4. Missing-mass-squared distribution for hypothesis (1.3), $K^-p \to p\pi^-$(MM), for all two-prong events with $0.0 < MM^2 < 0.5$ GeV^2.

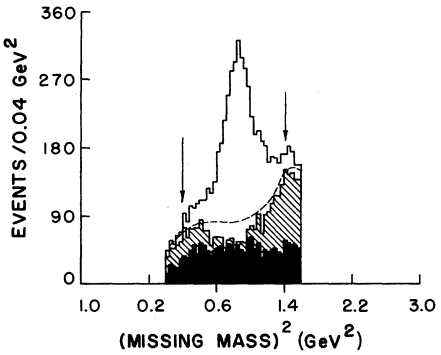

FIG. 5. Missing-mass-squared distribution for hypothesis (1.4), $K^-p \to K^-\pi^+$(MM), for two-prong events with $0.0 < \mathrm{MM}^2 < 1.6$ GeV^2.

B. Event Identification

We first discuss the selection of the four-constraint (4c) K^-p elastic scattering data and then consider the problems encountered in allocating events to the various one-constraint (1c) hypotheses.

1. *Elastic Events*

Figure 1(a) shows the distribution in missing mass squared, MM^2, when the events are interpreted as hypothesis (1.1). The plot contains all two-prong events in sample II and clearly shows a prominent peak centered close to zero with a width of about 0.002 GeV^2 which contains the elastic events. Since a large fraction of all two-prong events ($\sim 20\%$)[4] is attributable to the elastic hypothesis, the tail of this peak can give serious background problems to other hypotheses, in particular to hypothesis (1.2), $K^-p \to pK^-\pi^0$. The principal background to the elastic events, in turn, comes from reaction (1.2).

To minimize these problems and the bias in the sample of elastic events, we refer to Fig. 1(b)

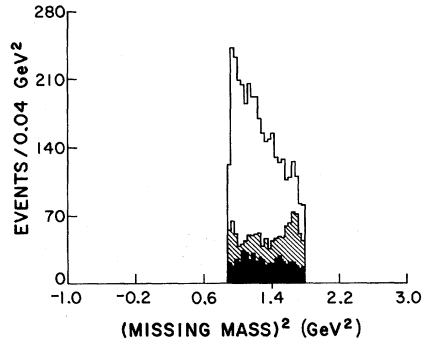

FIG. 6. Missing-mass-squared distribution for hypothesis (1.5), $K^-p \to \pi^-\pi^+$(MM), for two-prong events with $0.86 < \mathrm{MM}^2 < 1.80$ GeV^2.

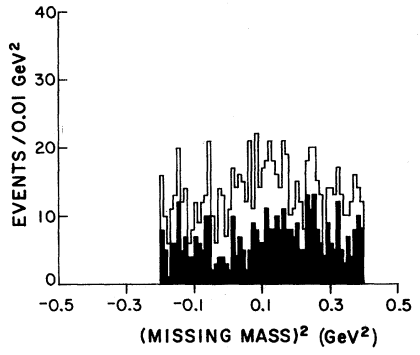

FIG. 7. Missing-mass-squared distributions for events with visible V^0 for (1.2). For Figs. 7–10, the shaded area corresponds to the events not satisfying criterion (a).

which shows the distribution in the missing mass squared defined as

$$\mathrm{MM}^2(p) = (P_K + P_p - P_p')^2,$$

where P_K, P_p, and P_p' are the four-momenta for incident K^-, the target proton, and the outgoing positive-charged particle assumed to be a proton, respectively. The dominant peak observed at the K-meson mass squared is again associated with elastic scattering; the peak observed at the $K^*(890)$ mass squared is due to the events from reactions (1.2) and (1.3). We note that the background to the elastic scattering events from reactions (1.2) and (1.3) is essentially removed for $\mathrm{MM}^2(p) < 0.5$ GeV^2. The shaded area in Fig. 1(a) corresponds to the events with $\mathrm{MM}^2(p) < 0$ or $\mathrm{MM}^2(p) > 0.5$ GeV^2 and does not show a peak at $\mathrm{MM}^2 \sim 0$.

The above arguments are summarized in Fig. 2, a scatter plot of MM^2 vs MM$^2(p)$ for a sample of events. This clearly demonstrates isolation of the 4c from the 1c events. The events are allocated to the elastic hypothesis by restricting both MM$^2(p)$ and MM^2 as shown in Fig. 2:

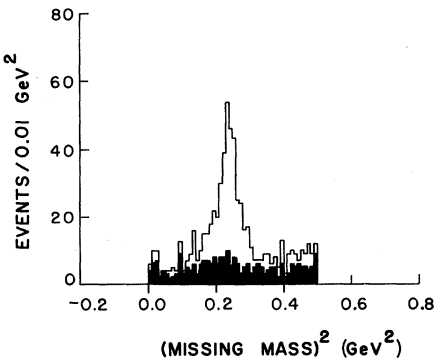

FIG. 8. Missing-mass-squared distributions for events with visible V^0 assuming hypothesis (1.3).

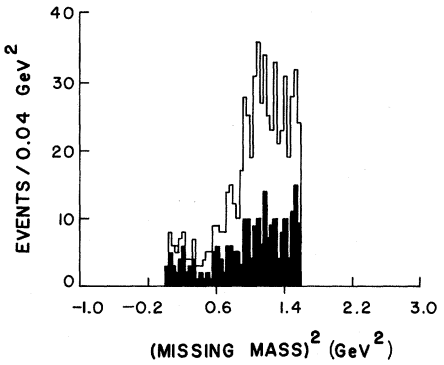

FIG. 9. Missing-mass-squared distribution for events with visible V^0 assuming hypothesis (1.4).

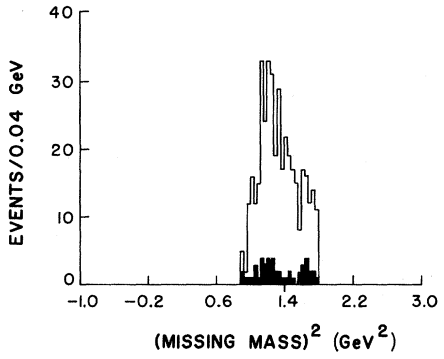

FIG. 10. Missing-mass-squared distribution for events with visible V^0 assuming hypothesis (1.5).

$0.0 < \mathrm{MM}^2(p) < 0.5$ GeV^2,

$-0.035 < \mathrm{MM}^2 < 0.025$ GeV^2.

The asymmetric cut in MM^2 takes account of the stronger tail effect in the negative missing-mass-squared region.

2. *One-Constraint Channels*

We show the missing-mass-squared distributions for hypotheses (1.2)–(1.5) in Figs. 3–6 after removing the elastic scattering events, as defined in Sec. II B 1, from sample II. There are strong signals corresponding to missing π^0, $\bar{K}^0$, and n in Figs. 3, 4, and 5, respectively. However, in Fig. 6, the signals corresponding to Λ^0 and Σ^0 production are masked by incorrectly identified neutron events, reaction (1.4). This indicates that $\Lambda^0(\Sigma^0)$ production through (1.5) is relatively weak compared to (1.4) as noted in the previous study of two-prong-plus-V^0 events at this energy.[1] The interest lies only in considering the contamination of events assigned to (1.4) by events from (1.5).

We first state the criteria to select the 1c fit events for (1.2), (1.3), and (1.4), and then discuss these in some detail:

(a) χ^2 probability for ionization fits > 0.01,

(b) χ^2 probability for kinematical fits > 0.05, and

(c) cuts in the missing mass squared;

$-0.05 < \mathrm{MM}^2 < 0.09$ GeV^2 for (1.2),

$0.18 < \mathrm{MM}^2 < 0.32$ GeV^2 for (1.3),

$0.52 < \mathrm{MM}^2 < 1.08$ GeV^2 for (1.4).

For each event, the predicted and measured ionization densities for visible tracks are used to compute an over-all ionization probability.[5] The shaded areas in Figs. 3–6 are those events which do not satisfy criterion (a); in all cases, removal of these events introduces no bias in the signal region. To further illustrate the consistency of the ionization selection, Figs. 7–10 show the missing-mass-squared distributions for reactions (1.2)–(1.5) using only those events overlapping with the two-prong-plus-V^0 events in sample I which, therefore, cannot belong to (1.2) or (1.4). The events with inconsistent ionization (shaded area in Figs. 7–10) again show smooth distributions and indicate that ionization criterion (a) does not cause any bias in the event selection. The shaded areas in Figs. 3 and 5 include these overlapping V^0 events in addition to those inconsistent with criterion (a).

TABLE I. Numbers of events selected from K^-p two-prong measurements (sample II) and ambiguity between reactions.

Reaction	Reaction number	Reaction number 1.1	1.2	1.3	1.4	1.5
$K^-p \to K^-p$	1.1	8970	...	...	...	...
$\to K^-p\pi^0$	1.2	...	1283	238	91	62
$\to \pi^-pK^0$	1.3	...		1592	92	57
$\to K^-\pi^+n$	1.4	...			2393	729
$\to \pi^-\pi^+\begin{pmatrix}\Lambda^0\\ \Sigma^0\end{pmatrix}$	1.5	...				1853

The cross-hatched areas in Figs. 3–6 indicate those events which fail to satisfy criterion (b). The 1c events are finally selected from the unshaded area in each figure with the appropriate missing-mass cut (c) imposed. The asymmetric missing-mass-squared cut for reaction (1.4) is to reduce the background from reaction (1.5) and from events having an additional π^0 from $\Delta^0(1236)$ decay. The numbers in the diagonal boxes in Table I are those selected for each reaction.

C. Ambiguities

The elastic events are removed from the sample as discussed previously. We consider here the ambiguities among 1c-fit hypotheses after the event selection described in Sec. II B 2. Table I shows the numbers of events with one kinematical constraint which are ambiguous between any two hypotheses as entries in the off-diagonal boxes. Less than 2% of events have acceptable fits to more than two hypotheses. Those final states involving the proton, (1.2) and (1.3), each have less than 100 events ambiguous with reactions (1.4) and (1.5). The major ambiguities occur between the two proton hypotheses (1.2) and (1.3) and also between (1.4) and (1.5).

Figure 11(a) shows the outgoing π^- laboratory momentum distribution for those two-prong-plus-V^0 events giving a satisfactory 4c fit to the final-state $\bar{K}^0 p\pi^-$. For comparison, we show the corresponding distribution for events selected as $\bar{K}^0 p\pi^-$ from the two-prong sample II. The cross-hatched area corresponds to the two-prong events ambiguous between hypotheses (1.2) and (1.3). Inclusion of the shaded events in Fig. 11(b) approximately reproduces the shape of the distribution in Fig. 11(a). We estimate that about 70% of the overlapping events actually belong to hypothesis (1.3), so that our assignment of all these events to hypothesis (1.3) in what follows results in rather small error.

A major part of the ambiguity for reaction (1.4) comes from events actually belonging to reaction (1.5). Figure 9 shows the missing-mass-squared distribution obtained assuming hypothesis (1.4) for those events known to have an associated V^0, but which were measured as two-prong events. The distribution rises sharply at a missing-mass-squared of about 0.9 GeV^2. The asymmetric missing-mass-squared cut made for (1.4) will then reduce the contamination from $\Lambda^0\pi^-\pi^+$ events. Applying the selection criteria for hypothesis (1.4), we obtained 124 events from the control sample of V^0 events. Since the ratio of events with unseen Λ^0 to those with seen Λ^0 is about unity in this bubble chamber, we estimate that about 120 $\Lambda\pi\pi$ events are included in the $K^-\pi^+ n$ sample. Thus, almost

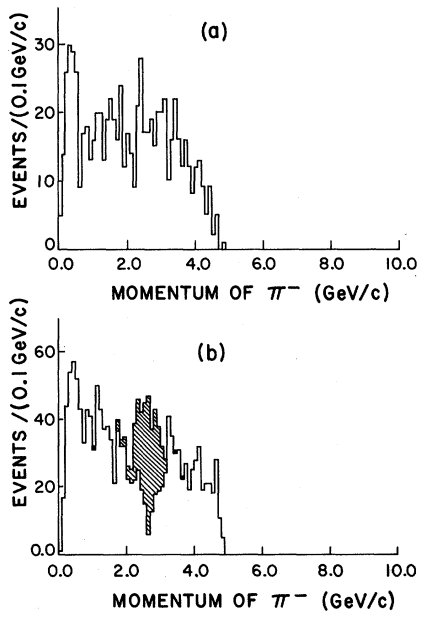

FIG. 11. Distributions of outgoing π^- laboratory momentum (a) for two-prong-plus-V^0 events with 4c fit for reaction (1.3) from sample I, and (b) for two-prong events fitting reaction (1.3). The shaded area corresponds to two-prong events ambiguous between hypotheses (1.2) and (1.3).

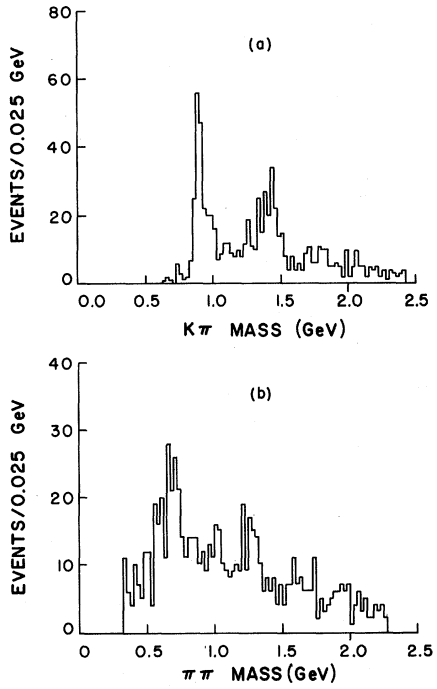

FIG. 12. Distributions of (a) the $K^-\pi^+$ and (b) the $\pi^-\pi^+$ mass for the events ambiguous between hypotheses (1.4) and (1.5).

TABLE II. Estimated numbers of events and channel cross sections.

Reaction	Event number estimated from missing mass	Cross section (mb)	Event number used from samples I and II
$K^- + p \to K^- p$	13183 ± 900	4.1 ± 0.3	8970
$\to K^- p\pi^0$	1503 ± 180	0.468 ± 0.056	1045
$\to \pi^- pK^0$	1450 ± 200	0.452 ± 0.060	2086
$\to K^- \pi^+ n$	2631 ± 240	0.883 ± 0.075	2875
Total	45890	14.3 ± 0.4	

all of the overlap between reactions (1.4) and (1.5) shown in Table I should be assigned to reaction (1.4). This is further demonstrated by showing the $K\pi$ mass distribution assuming (1.4) in Fig. 12(a) and the $\pi\pi$ mass distribution assuming (1.5) in Fig. 12(b) for these ambiguous events. We observe both strong $K^*(890)$ and $K^*(1420)$ signals in Fig. 12(a) at their expected positions, consistent with most of these events coming from (1.4). In contrast, the $\pi\pi$ mass distribution in Fig. 12(b) shows a peak at about 0.7 GeV, less than the ρ^0 mass by 0.06 GeV. This observation can, for the most part, be explained as a kinematical reflection of the $K^*(890)$.

III. CROSS SECTIONS

The cross sections for reactions (1.1) and (1.4) are obtained by using the 5.5-GeV/c $K^- p$ total cross section of 24.3 ± 0.8 mb measured in counter experiments[6] and the ratio of two-prong to total interactions. This ratio was obtained from a partial scan for all event topologies, with correction for the loss of elastic events with small angles as discussed in Sec. IIIA. The corrected value of this ratio is then

$$R = 0.595 \pm 0.018,$$

which gives a two-prong cross section

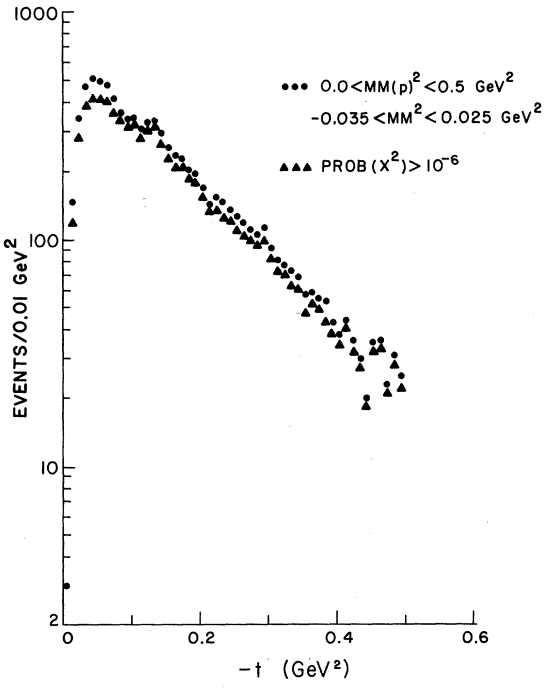

FIG. 13. t distributions for elastic events. The circular dot corresponds to events selected with $0.0 < \mathrm{MM}^2(p) < 0.5$ GeV^2 and $-0.035 < \mathrm{MM}^2 < 0.025$ GeV^2. The triangular dot corresponds to events with χ^2 probability greater than 10^{-6}.

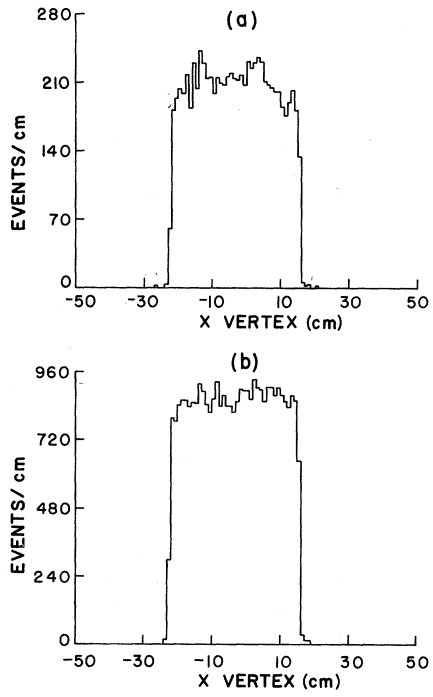

FIG. 14. X-vertex distributions for (a) events selected with $0.0 < \mathrm{MM}^2(p) < 0.5$ GeV^2 and $-0.035 < \mathrm{MM}^2 < 0.025$ GeV^2 and (b) for all other events giving a 1c fit.

TABLE III. Slopes for K^-p elastic differential cross section.

$\|t\|$ Range (GeV^2)	Function form	χ^2/NDF[a]	Slope B (GeV^{-2})	Slope C (GeV^{-4})	Forward cross-section optical point (mb/GeV^2)
0.12–0.68	e^{Bt}	$\frac{12}{7}$	-7.26 ± 0.13		27.7 ± 1.0
	e^{Bt+Ct^2}	$\frac{11}{6}$	-7.86 ± 0.58	0.94 ± 0.88	30.0 ± 2.4

[a]NDF ≡ number of degrees of freedom.

$\sigma_{2\text{-prong}} = 14.3 \pm 0.4$ mb.

The channel cross sections σ_i, calculated from sample II alone, are then given by

$$\sigma_i = \frac{N(i)}{N(2\text{-prong})} \times \sigma_{2\text{-prong}},$$

where $N(i)$ is the number of events for reaction (i) obtained from the corresponding missing-mass-squared distribution and N(2-prong) is the corrected total number of two-prong events. The numbers of events and the cross sections are given in Table II and we now discuss the various corrections involved in arriving at these values.

A. Elastic Events

It is claimed in Sec. II that the elastic events are clearly separated from all others by imposing appropriate restrictions on the missing masses, MM and MM(p). Events with a short stopping proton have a large scanning bias and are lost from this elastic-event sample; a correction is required to obtain the true number of events. This sample includes a small number of events which do not give a kinematically satisfactory fit, but nevertheless belong to the elastic category. Figure 13 shows the distribution in the squared four-momentum transfer t, dN/dt, for all events selected as elastic and separately for those which have a kinematical χ^2 probability greater than 10^{-6}. For $|t| > 0.12$ GeV^2, the slopes of these two distributions are the same. We then assume that a complete sample of elastic events is obtained by applying the above selection criteria and, in the following, we use all events which satisfy those criteria.

We first correct for the bias in the azimuthal angular distribution of the scattering plane about the beam direction for the events with $|t| > 0.12$ GeV^2. A correction of 3.6% is required to make this distribution isotropic.

To estimate the number of events in the forward region ($|t| < 0.12$ GeV^2), we fit the momentum-transfer distribution for $|t| > 0.12$ GeV^2, corrected in the above way, using the equation $dN/dt = Ae^{Bt+Ct^2}$. The corrected number of events with $|t| < 0.12$ GeV^2 is then given by the fitted curve, extrapolated to the forward direction. These scanning-loss effects are also seen in the distribution of the selected events over the fiducial volume. Figures 14(a) and 14(b) show the fiducial volume distribution along the beam direction for the elastic events and the one-constraint fitted events, respectively. An apparent loss of elastic events is observed at the downstream end of the chamber whereas the inelastic events do not show this effect. Finally, we estimate the correction for events excluded by the cuts in missing mass MM and MM(p) to be about 5% of the uncorrected total. The elastic cross section, including these correction factors, is 4.1 ± 0.3 mb, in agreement with a previous measurement at this momentum.[4]

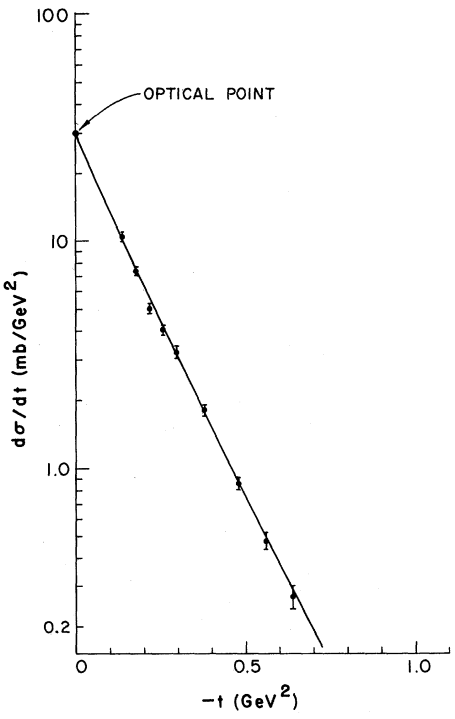

FIG. 15. Differential cross section $d\sigma/dt$ for elastic scattering. The curve is the fit with $d\sigma/dt = Ae^{Bt+Ct^2}$ in the $|t|$ range between 0.12 and 0.68 GeV^2.

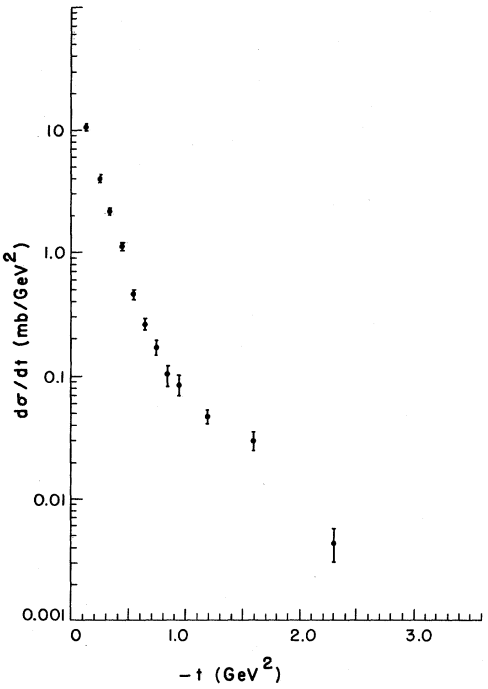

FIG. 16. Differential cross section $d\sigma/dt$ for elastic scattering for the $|t|$ range between 0.12 and 2.8 GeV^2.

B. One-Constraint Hypothesis

The number of events to be assigned to any 1c channel must be estimated from the corresponding missing-mass-squared distribution, taking into account the appropriate background. In view of the lack of a reliable formulation of this background level, we represent it by drawing a smooth curve on the missing-mass-squared distribution. The dashed curves in Figs. 3, 4, and 5 are our estimate of background levels for the corresponding hypotheses. For hypothesis (1.4), since the tails of the $\Delta^0(1236)$ and $\Lambda^0(\Sigma^0)$ peaks extend into the neutron missing-mass region, we expect to allow for this in drawing the background level. The number of events above these background levels in the missing-mass interval indicated by the arrows has been used to estimate the channel

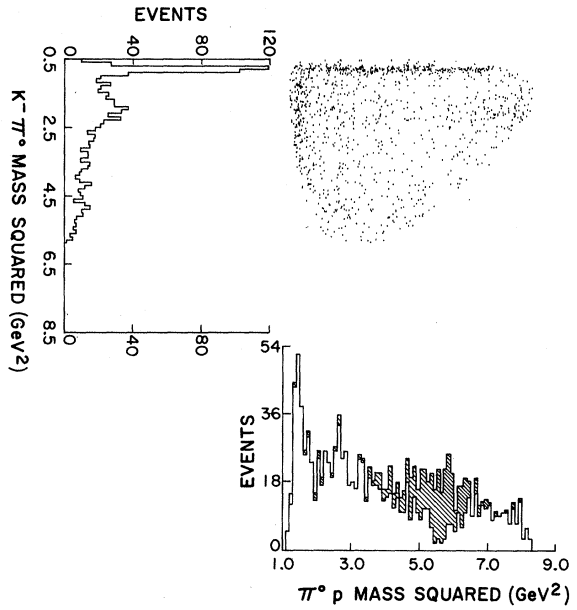

FIG. 17. Dalitz plot for reaction (1.2). The shaded area on the $p\pi^0$ mass projection corresponds to the events ambiguous between reactions (1.2) and (1.3).

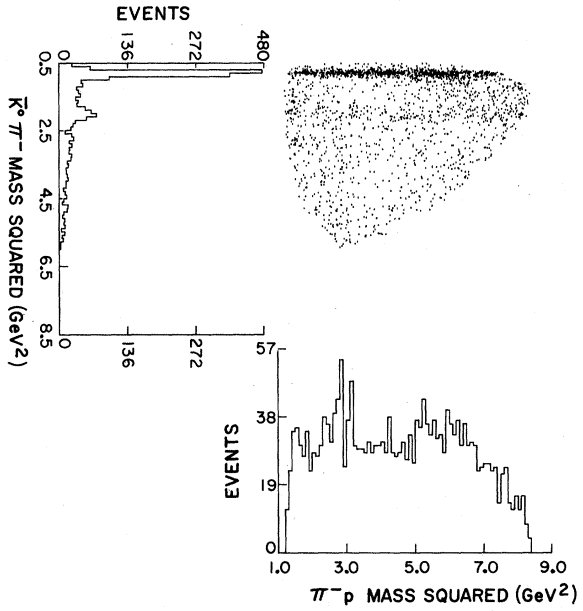

FIG. 18. Dalitz plot for reaction (1.3).

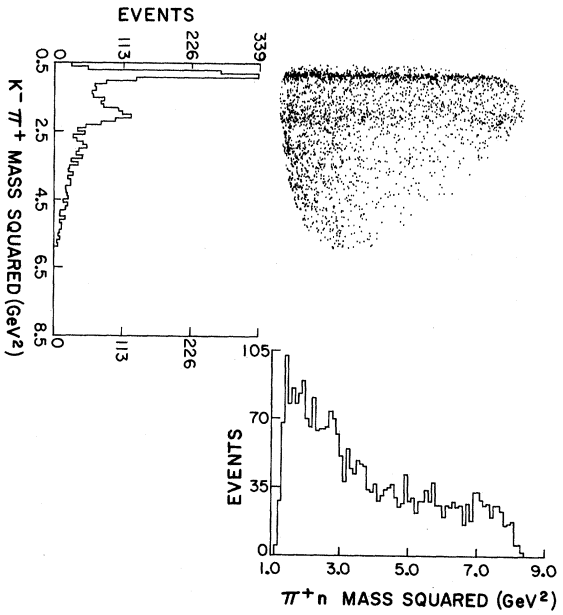

FIG. 19. Dalitz plot for reaction (1.4).

cross section.

Table II gives the channel populations with the corresponding cross sections. No scanning-loss correction has been made for events with a short stopping proton in reactions (1.2) and (1.3). However, this correction was estimated to be about 6% of the events assigned to the reaction $K^-p \to K^{*-}(890)p$.[7] The error quoted in Table II includes the estimated uncertainty in the background level. The cross sections for reactions (1.3) and (1.4) agree with those given in Ref. 1 within the errors.

IV. GENERAL FEATURES

A. K^-p Elastic Scattering

For elastic scattering, an azimuthal-angle correction has been made to the full $|t|$ range. However, as discussed in Sec. III A, there remains a substantial loss of events for $|t| < 0.12$ GeV^2. We have, therefore, used the data for $0.12 < |t| < 0.68$ GeV^2 in determining the slope of the differential cross section. The results given in Table III are obtained using a least-squares method to fit the data with the two functional forms

$$\frac{d\sigma}{dt} = \left(\frac{d\sigma}{dt}\right)_{t=0} e^{Bt} \tag{4.1}$$

and

$$\frac{d\sigma}{dt} = \left(\frac{d\sigma}{dt}\right)_{t=0} e^{Bt+Ct^2}. \tag{4.2}$$

Figure 15 shows $d\sigma/dt$ with the fitted curve of Eq. (4.2). The results obtained for the restricted $|t|$ range are consistent with those from previous measurement at this momentum.[4]

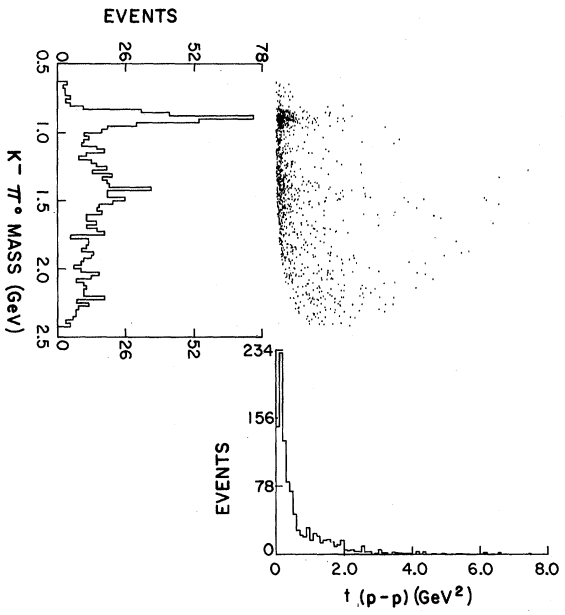

FIG. 20. Chew-Low plot for reaction (1.2).

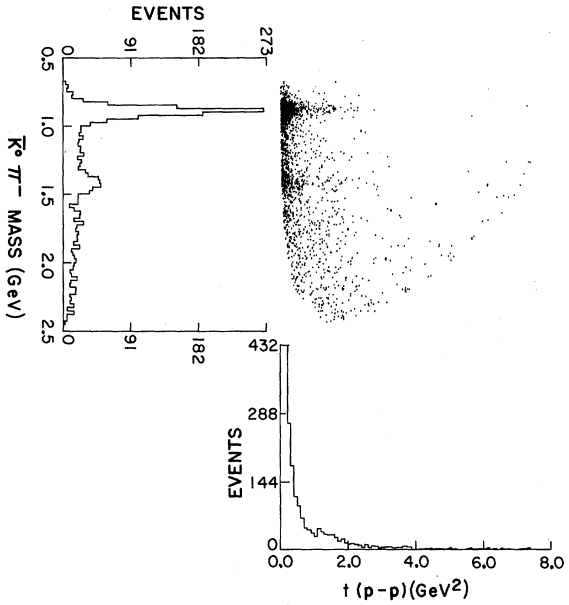

FIG. 21. Chew-Low plot for reaction (1.3).

The optical point, $(d\sigma/dt)_{t=0}$, is determined by extrapolating the fitted curve to $t=0$. Again, using the $|t|$ region from 0.12 to 0.68 GeV^2, this gives

$$\left(\frac{d\sigma}{dt}\right)_{t=0} = 30.0 \pm 2.4 \text{ mb/GeV}^2.$$

The optical point calculated from the K^-p total cross section is 29.4 mb/GeV^2, which is consistent with zero real part in the scattering amplitude.

Figure 16 shows $d\sigma/dt$ for the larger t region of $0.1 \leq |t| \leq 2.8$ GeV^2. Although our data are limited in statistics, there is an indication of a change of

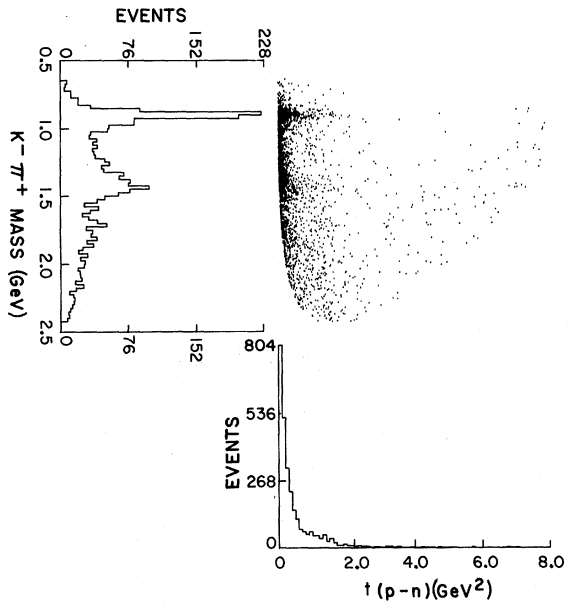

FIG. 22. Chew-Low plot for reaction (1.4).

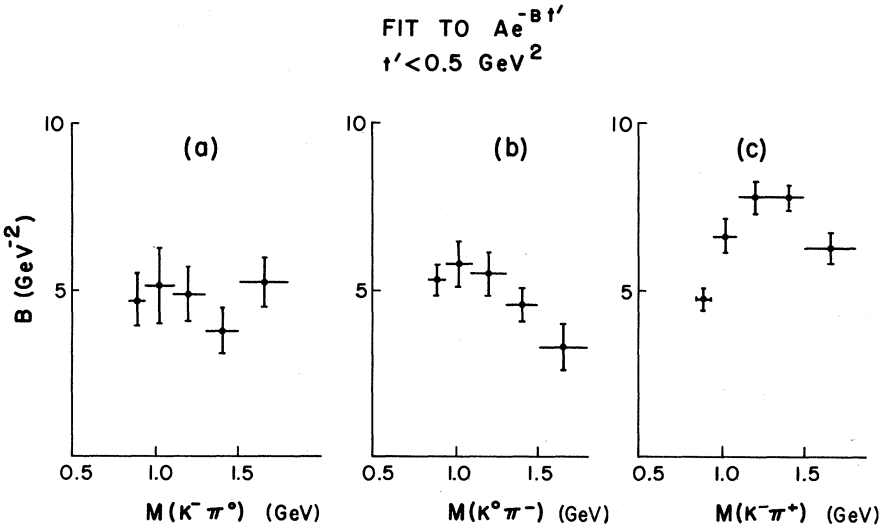

FIG. 23. Slopes in t' distributions as a function of $K\pi$ invariant mass: (a) for reaction (1.2), (b) for (1.3), and (c) for (1.4).

slope, or possibly a dip at about 1.0 GeV^2 which is consistent with other measurements.[8,9] We also note that no backward peak is observed in our data. Only two events are obtained with $|t| > 2.8$ GeV^2 corresponding to a cross section of less than 1 μb.

B. Single-Pion Production

Figures 17, 18, and 19 show Dalitz plots for reactions (1.2), (1.3), and (1.4), respectively. Strong $K^*(890)$ production is observed for each reaction with weaker production of the $K^*(1420)$ in each case. No other significant effects are observed in the $K\pi$ mass projections. The shaded events on the $p\pi^0$ mass projection in Fig. 17 correspond to those events ambiguous between reactions (1.2) and (1.3), and which have been assigned to reaction (1.3), as discussed in Sec. IIC. These events might be expected to produce a bias in the $K\pi$-scattering angular distribution. However, the removal of these events from reaction (1.2) gives rise to rather small changes, within the statistical uncertainty in the angular distribution.

A strong $\Delta(1236)$ signal is observed in reaction (1.2), whereas its production in reactions (1.3) and (1.4) is much weaker. The πN effective-mass distributions in Figs. 17 and 19 show a broad enhancement at low πN masses which does not appear in Fig. 18. This difference can be understood in terms of strong diffractive πN production in the case of reactions (1.2) and (1.4), where the pion emitted by nucleon dissociation interacts with the incident K^- diffractively, whereas this does not occur for reaction (1.3). We also note that no significant Y^* production is observed in any of these reactions (not shown).

Figures 20–22 show Chew-Low plots for these reactions. We observe pronounced event concentrations along the lower Chew-Low boundaries for all these reactions indicating the extremely peripheral nature of $K^*(890)$ and $K^*(1420)$ production. Each of the plots indicates some forward nucleon scattering in association with high $K\pi$ mass. However, these events could be, in whole or part, a result of contamination from other reactions because of the ionization ambiguity between a fast π^+ and a proton.

To show the slope of $d\sigma/dt$ as a function of $K\pi$ mass, we fit $dN/dt' = Ae^{Bt'}$ to the t' distribution over the range of $t' < 0.5$ GeV^2, where t' is defined

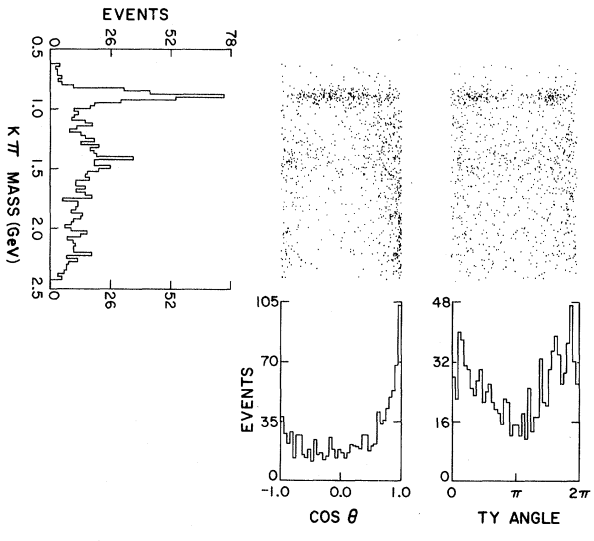

FIG. 24. Scatter plots of the $K\pi$ decay angles, cosθ and ϕ, in the Jackson frame vs $K\pi$ mass for reaction (1.2).

by $t' = |t - t_{\min}|$ and $t_{\min}$ is the kinematical minimum value of t for a given $K\pi$ mass. The results of these fits are shown in Fig. 23 for the three reactions. The slope, B, for the $K^*(890)$ mass region is about 5 GeV^{-2} in each case. It is interesting to note that the slopes for the $K^{*-}(890)$, known to be produced through vector exchange, are the same as that for $\overline{K}^{*0}$ production where pion exchange is dominant. We also note that B for reactions (1.2) and (1.3) is almost constant, whereas B for reaction (1.4) increases as the $K\pi$ mass increases and finally falls off.

Figures 24–26 show scatter plots of $\cos\theta$ and ϕ as a function of $K\pi$ mass, where θ and ϕ are the polar and azimuthal angles of the outgoing K meson with respect to the incident K in the $K\pi$ rest frame (Jackson frame); in each case all events are used without restriction on t. These figures reveal strikingly contrasting features in the angular correlations of the $K\pi$ system produced in the three reactions. At low $K\pi$ mass, the $K^*(890)$ region, the $(K\pi)^-$ systems of reactions (1.2) and (1.3) show very similar $\sin^2\theta$ distributions in contrast to the $\cos^2\theta$ dependence in reaction (1.4). We note that in all three cases, the Treiman-Yang angular distributions are markedly anisotropic with a strong $\cos 2\phi$ component. At higher $K\pi$ masses, most strikingly above 1.4 GeV, the angular distributions for (1.2) and (1.4) show strong forward peaks consistent with the dominance of $K\pi$ diffractive scattering. In contrast, no forward peak is observed in (1.3), where $K\pi$ diffractive scattering cannot occur.

C. Resonance Parameters for the $K^*(890)$ and $K^*(1420)$

We have analyzed the $K\pi$ mass spectra, plotted in 20-MeV bins, over the complete $K\pi$ mass range to find the production cross section, mass, and width of both the $K^*(890)$ and the $K^*(1420)$ in reactions (1.2)–(1.4). Using a least-squares method, we have fitted these spectra to a functional form of the $K\pi$ mass, m:

$$F(m) = \mathrm{PS}(m)\left(a + \sum_{i=1}^{2} f_i \mathrm{BW}_i(m)\right), \tag{4.3}$$

where the parameters a and f_i, respectively, represent the fractions of background and the ith resonance. $\mathrm{BW}_i(m)$ is the Breit-Wigner form for the ith resonance with mass m_i, width Γ_i, and spin l_i, written as[10]

$$\mathrm{BW}_i(m) = \frac{m}{q}\,\frac{\Gamma_i}{(m^2 - m_i^2)^2 + m_i^2\Gamma_i^2}, \tag{4.4}$$

with $\Gamma_i = \Gamma_0(q/q_i)^{2l_i+1}$, where q and q_i are the $K\pi$ center-of-mass momenta of the decay products for $K\pi$ mass m and m_i (resonant mass), respectively. We have tried both Lorentz-invariant phase space and a fifth-order polynomial form for the background shape, $\mathrm{PS}(m)$.[11] Since our data are limited in statistics, we are not able to obtain a reasonable width for the $K^*(1420)$. The resonant mass

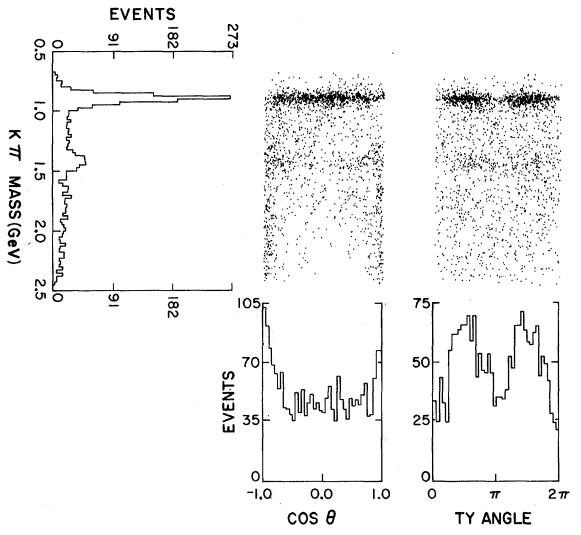

FIG. 25. Scatter plots of the $K\pi$ decay angles, $\cos\theta$ and ϕ, in the Jackson frame vs $K\pi$ mass for reaction (1.3).

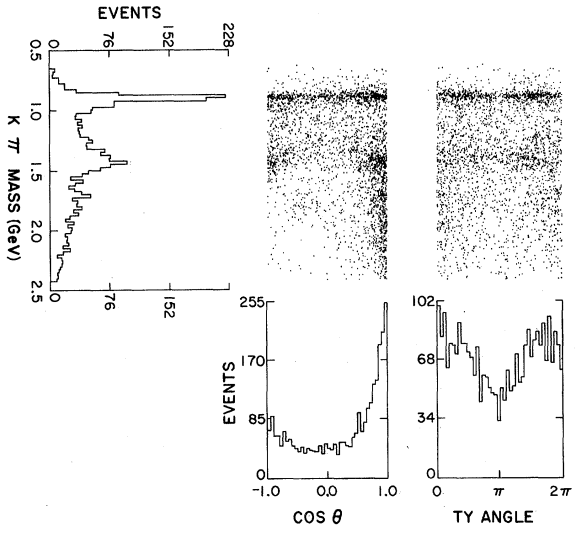

FIG. 26. Scatter plots of the $K\pi$ decay angles, $\cos\theta$ and ϕ, in the Jackson frame vs $K\pi$ mass for reaction (1.4).

TABLE IV. Resonance parameters for the $\overline{K}^*(890)$ and the $\overline{K}^*(1420)$. The values in parentheses correspond to the results obtained from the use of the phase-space form of PS(m).

$K^*(890)$ decay	$K^-\pi^0$	$\overline{K}^0\pi^-$	$K^-\pi^+$
Cross section (μb)	140 ±16	224 ±31	237 ±22
	(109.5±19)	(193 ±26)	(235 ±21)
Mass (MeV)	888.5± 2.9	891.3± 1.3	898.8± 1.5
	(888.3± 2.9)	(891.5± 1.3)	(900.1± 1.4)
Width (MeV)	59 ±12	54 ± 5	47 ± 6
	(50 ± 8)	(52 ± 3)	(49 ± 4)
Fraction (%)	27.7± 2.3	48.6± 1.8	26.8± 1.3
	(23.4± 2.3)	(42.6± 1.9)	(26.7± 1.3)
$K^*(1420)$ decay	$K^-\pi^0$	$\overline{K}^0\pi^-$	$K^-\pi^+$
Cross section (μb)	48 ± 6	52 ± 6	108 ±11
	(42 ± 6)	(45 ± 6)	(132 ±13)
Mass (MeV)	1426 ±11	1425 ± 7	1424 ± 6
	(1425 ±13)	(1422 ± 7)	(1418 ± 5)
Fraction (%)	10.3± 2.1	11.5± 1.4	12.2± 1.2
	(9.0± 2.0)	(10.0± 1.3)	(15.0± 1.3)

and the fraction of $K^*(1420)$ were determined, in each case, using a fixed width of 100 MeV.

Table IV gives the results of these fits. The values in parentheses correspond to the results obtained from the use of the phase-space form of PS(m). The quoted errors in masses, widths, and fractions are only statistical. As seen in this table, the fitted values depend on the form of PS(m) used. However, the differences in these values are generally within the errors. Further discussion of the $K^*(890)$ mass determination will be given in Sec. V. Since the fit with the polynomial form of PS(m) gives a slightly better χ^2 than that with the phase-space form, we use the results obtained from the former fit. The curves in Figs. 27–29 are obtained from this fit.

The production cross sections of the $K^*(890)$ and the $K^*(1420)$ are obtained from the channel cross sections in Table II combined with the resonant fractions obtained in the above fit. For the $K^{*-}(890)$ cross sections, a correction has been made for the loss of short stopping protons in scanning.[7] The quoted errors include the fractional uncertainties in the channel cross sections, which are much higher than the statistical errors in each case. The ratio of the $K^{*-}(890)$ production cross section in reaction (1.2) to that in (1.3) is 0.62 ± 0.11, using the fit results obtained assuming the polynomial background form. This result is consistent with the value of 0.5 expected from isospin conservation in the $K^{*-}(890)$ decay.

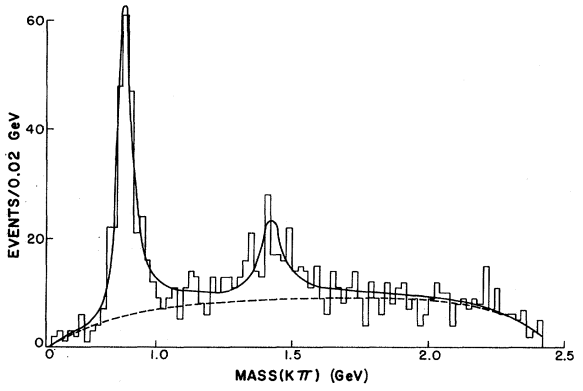

FIG. 27. $K^-\pi^0$ mass spectrum plotted in 20-MeV bins. For Figs. 27–29, the solid and dashed curves are the results of the fits representing the resonant $K\pi$ mass spectra and the fifth-order polynominal background, respectively.

V. PROPERTIES OF THE $\overline{K}^*(890)$

A. $\overline{K}^{*0}(890)$-$K^{*-}(890)$ Mass Difference

The charged and neutral $K^*(890)$ states may be expected to have slightly different masses as a re-

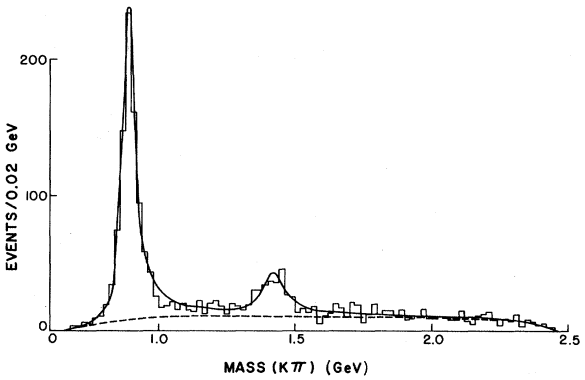

FIG. 28. $\overline{K}^0\pi^-$ mass spectrum plotted in 20-MeV bins. Curves as in Fig. 27.

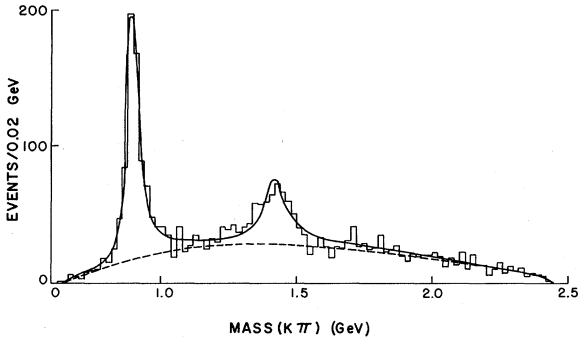

FIG. 29. $K^-\pi^+$ mass spectrum plotted in 20-MeV bins. Curves as in Fig. 27.

sult, first, of different electromagnetic effects in the two cases and, second, because of different interference effects between the $K^*(890)$ and the background amplitudes for the two cases. Since the interference with background such as an $I=\frac{3}{2}$ p-wave component can also cause a mass difference of a few MeV in the charged $K^{*-}(890)$ mass measured from its two different decay modes, we show the neutral-charged mass difference of the $K^*(890)$ separately for these two cases, as given in Table IV:

$$\Delta M_1 = M_{\bar{K}^{*0}(890)\to K^-\pi^+} - M_{K^{*-}(890)\to \bar{K}^0\pi^-}$$
$$= 7.5 \pm 2.0 \text{ MeV},$$
$$\Delta M_2 = M_{\bar{K}^{*0}(890)\to K^-\pi^+} - M_{K^{*-}(890)\to K^-\pi^0}$$
$$= 10.3 \pm 3.3 \text{ MeV}.$$

These are in agreement within the statistical errors and are consistent with other reported values.[12,13]

There are several systematic effects which could be important in this method of determining the neutral-charged mass difference. We use the mass interval $0.7 \leq M(K\pi) \leq 1.1$ GeV and choose a linear form[14] for PS(m) in Eq. (4.3) to estimate the magnitude of these effects. Table V summarizes the effects on the $K^*(890)$ mass of varying the mass binning, the Breit-Wigner form used, and the four-momentum-transfer range considered. There are differences of the order of 1 standard deviation from those values given in Table IV. Table V shows that both of the charged $K^{*-}(890)$ mass measurements increase by as much as 2 MeV, whereas the neutral $\bar{K}^{*0}(890)$ mass remains almost the same compared to values in Table IV.

It is possible to introduce a systematic mass shift through the difference in the kinematical fitting between the proton hypotheses [(1.2) and (1.3)] and the neutron hypothesis (1.4). A sample of $\pi^- p\bar{K}^0$ events with seen V^0 and $K\pi$ mass less than 1.0 GeV were measured as two-prong-plus-V events and fitted in two ways: (1) with one constraint, without making use of the V^0 track, and (2) with one constraint, making use of the measured V^0 tracks but not the proton track. The first case corresponds to hypothesis (1.3) and the second corresponds to a simulated fit to hypothesis (1.4) where only visible boson tracks are used in the fit as in (1.4). The difference between the $K\pi$ invariant-mass peaks obtained in the above two ways was 0.8 ± 0.6 MeV, with the first method producing the higher mass. The total systematic error in ΔM_1 and ΔM_2 from the effects considered here could be as large as 3 MeV with the major part due to ignorance of the background shape.

Recently, Berger and Fox[15] have calculated the K^* mass shift due to interference with Δ-production background using a B_5 model and found the $K^{*-}(890)$ mass to shift down by about 2 MeV from the mass value without interference, while no shift is obtained in the $K^{*0}(890)$ mass. We calculate the shifts in $K^*(890)$ mass resulting from interference with an $I=\frac{3}{2}$ p-wave background represented by the appropriate $K\pi$ phase shifts, as predicted by Lovelace,[16] to be 2.5, −0.5, and 1.0 MeV, respectively. Thus, the experimentally observed mass differences, ΔM_1 and ΔM_2, easily encompass the shifts due to the interference effects. We also note that a calculation by Rubinstein[17] within the framework of SU(6) shows

TABLE V. $K^*(890)$ mass shifts.

Breit-Wigner form	Bin size (GeV)	Starting Bin (GeV)	$\lvert t\rvert$ Range (GeV^2)	Mass for $K^{*-}(890)\to K^-\pi^0$ (MeV)	Mass for $K^{*-}(890)\to \bar{K}^0\pi^-$ (MeV)	Mass for $\bar{K}^{*0}(890)\to K^-\pi^+$ (MeV)
p-wave	0.020	0.600	All	890.9 ± 3.6	893.2 ± 1.6	898.5 ± 1.6
s-wave	0.020	0.600	All	888.8 ± 3.3	891.6 ± 1.5	898.6 ± 1.6
p-wave	0.020	0.610	All	891.5 ± 3.3	894.1 ± 1.6	898.3 ± 1.6
p-wave	0.025	0.600	All	889.9 ± 3.6	893.1 ± 1.6	897.8 ± 1.6
p-wave	0.020	0.600	$\lvert t\rvert < 0.1$	887.4 ± 5.6	892.1 ± 3.2	898.3 ± 1.9
p-wave	0.020	0.600	$\lvert t\rvert > 0.1$	894.4 ± 4.4	893.4 ± 1.8	898.7 ± 1.9
			Average	890.5 ± 3.3	892.9 ± 1.6	898.4 ± 1.6

TABLE VI. Differential cross sections for reaction $K^-p \to \bar{K}^{*0}p$.

$\lvert t\rvert$ Range (GeV^2)	Corrected number of events/0.04 GeV^2	For $K^-\pi^+$ decay ($\mu\mathrm{b}/\mathrm{GeV}^2$)	Cross section corrected for other decay modes ($\mu\mathrm{b}/\mathrm{GeV}^2$)
0.003–0.04	95 ±10.0	958±102	1437±153
0.04 –0.08	78 ± 8.8	790± 89	1185±134
0.08 –0.12	59 ± 7.7	598± 78	897±117
0.12 –0.16	45 ± 6.7	456± 68	684±102
0.16 –0.20	42 ± 6.5	425± 66	638± 99
0.20 –0.28	31.6± 4.0	320± 40	480± 60
0.28 –0.36	21.5± 3.5	228± 35	342± 53
0.36 –0.52	13.5± 1.8	137± 18	205± 27
0.52 –0.68	7.5± 1.6	76± 16	114± 24
0.68 –1.00	4.0± 0.7	41± 7	61± 11
Total	585 events	237± 22 μb	355± 33 μb

$$M(K^{*0}) - M(K^{*-}) = M(K^0) - M(K^-)$$
$$= 3.95 \pm 0.13 \text{ MeV},$$

a smaller mass difference than the results given here by about 2 standard deviations.

B. Production and Decay of the $\bar{K}^{*0}(890)$

The neutral $\bar{K}^{*0}(890)$ produced in the reaction

$$K^-p \to \bar{K}^{*0}(890)n$$
$$\searrow K^-\pi^+ \qquad (5.1)$$

is studied using the sample of events from reaction (1.4) with $K\pi$ mass in the range $0.84 < M(K\pi) < 0.94$ GeV, which includes approximately 14% background. The differential cross section for $\bar{K}^*(890)$ production, $d\sigma/dt$, tabulated in Table VI, is obtained by normalizing the 585 events in this mass interval to the production cross section in Table IV.

Figure 30 shows $d\sigma/dt$ corrected for unseen decay modes of the $\bar{K}^{*0}(890)$. The solid and dashed curves are, respectively, the predictions of a one-

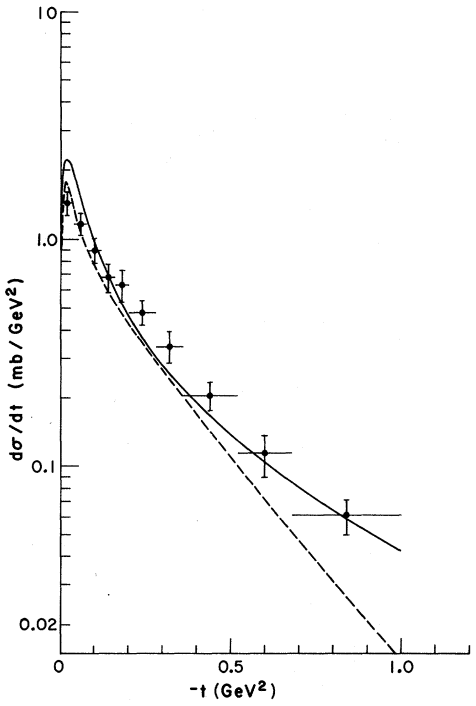

FIG. 30. Differential cross section for $K^-p \to \bar{K}^{*0}(890)n$. The corrections for unobserved decay modes are included.

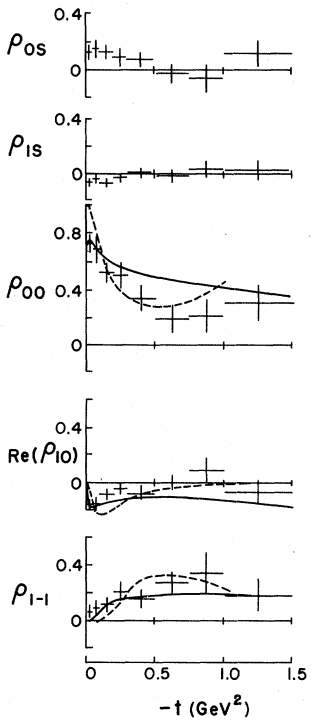

FIG. 31. Density-matrix elements for the $\bar{K}^{*0}$ decay in the Jackson frame.

TABLE VII. Density-matrix elements for the $\bar{K}^{*0}(890)$ evaluated in the Jackson frame.

$\|t\|$ Range (GeV^2)	Events $d\sigma/dt$ ($\mu b/GeV^2$)	Jackson frame ρ_{s0}	ρ_{s1}	ρ_{00}	ρ_{11}	$Re\rho_{10}$	ρ_{1-1}
0.003–0.05	119 (1536 ±140)	0.128±0.062	−0.062±0.026	0.733±0.070	0.133±0.035	−0.159±0.042	0.063±0.047
0.05 –0.10	77 (934 ±106)	0.154±0.062	−0.035±0.033	0.689±0.095	0.156±0.047	−0.153±0.048	0.091±0.055
0.10 –0.20	116 (704 ± 65)	0.130±0.050	−0.068±0.028	0.522±0.069	0.239±0.035	−0.086±0.042	0.118±0.055
0.20 –0.30	72 (437 ± 51)	0.093±0.064	−0.028±0.034	0.501±0.095	0.249±0.047	−0.041±0.045	0.212±0.069
0.30 –0.50	83 (252 ± 28)	0.076±0.055	0.055±0.035	0.337±0.088	0.332±0.044	−0.080±0.047	0.159±0.067
0.50 –0.75	45 (109 ± 16)	−0.025±0.069	−0.018±0.046	0.190±0.102	0.405±0.051	0.000±0.052	0.275±0.076
0.75 –1.00	24 (58 ± 12)	−0.059±0.095	0.031±0.060	0.211±0.117	0.395±0.059	0.092±0.093	0.345±0.147
1.00 –1.50	26 (31.6± 6.3)	0.122±0.095	0.025±0.063	0.308±0.125	0.346±0.063	−0.067±0.090	0.184±0.118

particle-exchange model incorporating absorptive effects (OPEA)[18,19] and a pure Regge model due to Dass and Froggatt.[20] In OPEA, we consider only pion exchange with the absorption parameters[19] $\gamma_i = 0.0284$, $C_i = 0.6456$, $\gamma_f = \frac{2}{3}\gamma_i$, and $C_f = 1.0$. In the Regge model, π and A_2 exchanges are included and the evasive solution (the dashed curve) is presented in Fig. 30.

The OPEA prediction of the production cross section is 371 μb, to be compared with 355±33 μb obtained from this experiment. However, the $d\sigma/dt$ predicted by both models gives a rather steeper distribution than indicated by the data.

The $K^*(890)$ decay characteristics are illustrated by plotting the density-matrix elements for the K^* decay, measured in the Jackson frame, as a function of t in Fig. 31. The matrix elements are calculated from the spherical-harmonic moments of the decay angular distribution expressed in terms of an s- and p-wave parametrization. In this parametrization, the density-matrix elements and the $\langle Y_l^m \rangle$ moments are related as follows:

$$\mathrm{Re}(\rho_{s0}) = \sqrt{\pi}\,\langle Y_1^0 \rangle,$$

$$\mathrm{Re}(\rho_{s1}) = \sqrt{\pi}\,\langle \mathrm{Re}(Y_1^1) \rangle,$$

$$\rho_{00} - \rho_{11} = \sqrt{5\pi}\,\langle Y_2^0 \rangle,$$

$$\mathrm{Re}(\rho_{10}) = (5\pi/3)^{1/2} \langle \mathrm{Re}(Y_2^1) \rangle,$$

$$\rho_{1-1} = -(10\pi/3)^{1/2} \langle \mathrm{Re}(Y_2^2) \rangle,$$

with the normalization conditions

$$\rho_{00} + 2\rho_{11} + \rho_{ss} = 1,$$

where ρ_{ss} represents the s-wave contribution to the angular distribution. The ρ_{00} and ρ_{11} elements appropriate to a pure p-wave parametrization are calculated from the value of $\rho_{00} - \rho_{11}$ and the normalization condition obtained by setting the diagonal element $\rho_{ss} = 0$, since no information on ρ_{ss} is available from the $\langle Y_l^m \rangle$ moments. However, some amount of s-wave component exists in the $K^*(890)$ mass region, as seen in the distribution of ρ_{s0}, which represents the s-p wave interference. The elements ρ_{00}, $\mathrm{Re}(\rho_{10})$, and ρ_{1-1} are compared to

TABLE VIII. Density-matrix elements for the $\bar{K}^{*0}(890)$ evaluated in the helicity frame.

$\|t\|$ Range (GeV^2)	Events	Helicity frame ρ_{s0}	ρ_{s1}	ρ_{00}	ρ_{11}	$Re\rho_{10}$	ρ_{1-1}
0.003–0.05	119	0.147±0.055	0.017±0.026	0.783±0.073	0.108±0.037	−0.73 ±0.039	0.088±0.048
0.05 –0.10	77	0.138±0.064	−0.061±0.035	0.606±0.081	0.197±0.011	−0.225±0.066	0.049±0.066
0.10 –0.20	116	0.150±0.044	−0.040±0.032	0.327±0.071	0.336±0.036	−0.163±0.037	0.020±0.060
0.20 –0.30	72	0.063±0.050	−0.052±0.044	0.116±0.076	0.442±0.038	−0.123±0.048	0.020±0.081
0.30 –0.50	83	−0.004±0.051	−0.052±0.038	0.212±0.074	0.394±0.037	−0.082±0.046	0.096±0.081
0.50 –0.75	45	0.032±0.064	0.014±0.049	0.108±0.089	0.446±0.044	−0.00 ±0.049	0.233±0.091
0.75 –1.00	24	−0.015±0.091	0.041±0.063	0.140±0.140	0.430±0.090	0.106±0.090	0.309±0.135
1.00 –1.50	26	−0.081±0.083	−0.069±0.071	0.102±0.126	0.449±0.063	0.019±0.083	0.081±0.126

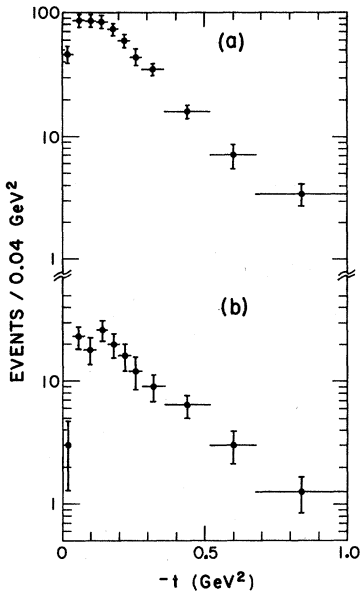

FIG. 32. Four-momentum-transfer-squared distribution (a) for reactions (5.3) and (b) for (5.2).

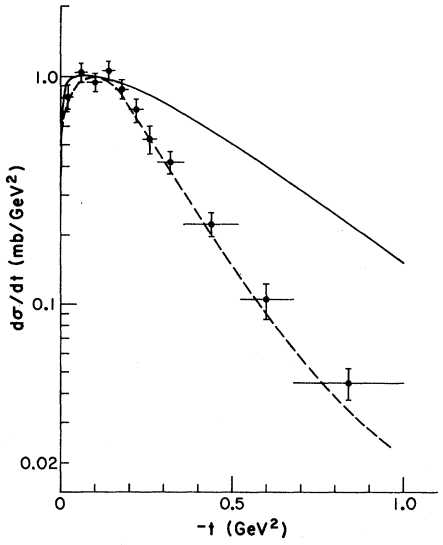

FIG. 33. Differential cross section for reaction $K^-p \to K^{*-}(890)p$ for all decay modes.

the model predictions. The solid and dashed curves are, respectively, the predictions of the OPEA and the Regge model for ρ_{00}, $\mathrm{Re}(\rho_{10})$, and ρ_{1-1} and again give reasonable agreement with the data. The experimental density-matrix elements, evaluated in both the Jackson and the helicity frames,[21] are given in Tables VII and VIII, respectively.

In conclusion, we remark that OPEA with pure pion exchange is in reasonable agreement with the data for the neutral $\overline{K}^{*0}(890)$. The Regge model with inclusion of π and A_2 exchange also gives a reasonable description of the data. However, both predictions show deviations from the data in the detailed features. Further study of the charge-exchange mechanism of $\overline{K}^{*0}$ production[22] suggests that a detailed comparison with the reaction $K^+n \to K^{*0}(890)p$ over a wide range of beam momenta is needed to understand the exchange mechanism of $K^{*0}(890)$ production.

C. Production and Decay of the $K^{*-}(890)$

The charged $K^{*-}(890)$ is produced in the reactions

$$K^-p \to K^{*-}(890)p, \quad K^{*-} \to K^-\pi^0 \tag{5.2}$$

and

$$K^-p \to K^{*-}(890)p, \quad K^{*-} \to \overline{K}^0\pi^- \tag{5.3}$$

which are first analyzed separately because of a different scanning bias in the small-t region for the two cases. Figures 32(a) and 32(b) show the

TABLE IX. Differential cross section for reaction $K^-p \to \overline{K}^{*-}(890)p$ (all decay modes).

$\lvert t\rvert$ Range (GeV²)	No. of events/0.04 GeV²	Cross section (μb/GeV²)
0.003–0.04	83 ±12.0	805±110
0.04 –0.08	109 ±10.4	1038±100
0.08 –0.12	103 ±10.1	950± 95
0.12 –0.16	110 ±10.5	1073±102
0.16 –0.20	93 ± 9.6	890± 87
0.20 –0.24	75 ± 8.7	718± 83
0.24 –0.28	56 ± 7.4	535± 72
0.28 –0.36	44 ± 4.7	418± 45
0.36 –0.52	22.3± 2.4	225± 24
0.52 –0.68	10.0± 1.5	105± 17
0.68 –1.00	4.6± 0.8	45± 7
Total	940 events	364± 35 μb

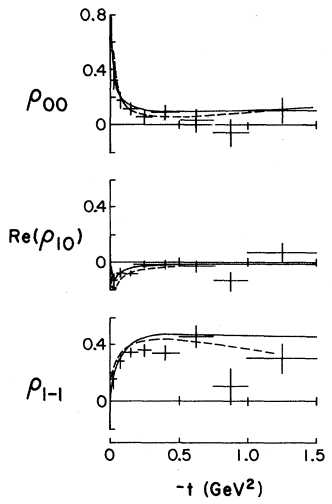

FIG. 34. Density-matrix elements for the $K^{*-}(890)$ evaluated in the Jackson frame.

momentum-transfer-squared distribution for (5.2) and (5.3), respectively. The mass bands used to select the $K^{*-}(890)$ events in (5.2) and (5.3) are the same as for the $\overline{K}^{*0}(890)$, and the background is estimated to be about 10%. The two distributions agree very well in shape for $|t| \geq 0.1$ GeV^2. For $|t| \lesssim 0.1$ GeV^2, the turnover in the differential cross section is more pronounced for reaction (5.2), where the events come only from the two-prong sample, than for (5.3), where some 30% of the events have a visible K^0 decay. This difference is attributed to a scanning loss associated with the short, stopping proton track. Since the only significant difference between the data is for small $|t|$, we combined these data in studying the $K^{*-}(890)$ production and decay properties. A correction for the scanning loss in the small-$|t|$ region was made for the two-prong events by a comparison of their $d\sigma/dt$ with that for the visible V^0 events for (5.3). The distribution in four-momentum transfer for $K^{*-}(890)$ production appears in Table IX and again in Fig. 33.

Figure 34 shows the density-matrix elements for the $K^{*-}(890)$ evaluated in the Jackson frame. The density-matrix elements evaluated in both the Jackson and the helicity frames are also given in Tables X and XI, respectively. The ρ_{s0} and ρ_{s1} representing the s- and p-wave interference are not given for the combined data for the $K^{*-}(890)$ because the s-wave background is expected to be different between reactions (5.2) and (5.3). We compare the combined data to the predictions of the same two models as previously used for the $\overline{K}^{*0}(890)$. The solid and dashed curves in Fig. 33 represent the predictions of OPEA[19,23] and the Regge model,[20] respectively. In the OPEA calculation, π and ω exchanges are included with the coupling-constant parameters given in Ref. 23. In the Regge model, π and P'' exchanges are considered; no ω exchange is included because of strong violation of SU(3) symmetry.[20] Both predictions in Fig. 33 (solid and dashed curves) are normalized to 1.0 mb/GeV^2 at $t = -0.1$ GeV^2 to compare the shape with the data. The normalization factors are 1.5 for the OPEA model and 1.2 for the Regge model. As reported[23,24] previously, the OPEA model does not describe the shape of $d\sigma/dt$ very well, but provides reasonable agreement with the experimental density-matrix elements, Fig. 34. In contrast, the Regge model describes both adequately. We also note that the Regge model with π and ω exchange[25] (not shown) gives reasonable descriptions of both the shape of $d\sigma/dt$ and the decay correlations.

D. Comparison of $\overline{K}^{*0}(890)$ and $K^{*-}(890)$

As already pointed out, the slope of $d\sigma/dt$ is very similar at $|t|$ values greater than 0.2 GeV^2 for both charged and neutral $\overline{K}^*(890)$. However, these distributions differ significantly in the small-momentum-transfer region. In the case of $K^{*-}(890)$, one sees the characteristic turnover associated with a vector-meson-exchange process. A much sharper distribution is obtained in the forward direction for $\overline{K}^{*0}(890)$ production.

To the extent that A_1 and B exchanges are negligible, ρ_{00} gives the contribution of one-pion exchange, with the $K^*(890)$ produced in the helicity-zero state. As shown in Tables VIII and XI, the value of ρ_{00} increases sharply in the forward direction for both neutral and charged $K^*(890)$ and becomes the dominant effect in the former case.

In the absence of absorptive effects, the density-matrix elements with nonzero helicity, such as ρ_{11}, indicate the contribution of vector-meson-exchange processes to $K^*(890)$ production. Furthermore, the following combinations[26] of density-matrix elements evaluated in the helicity frame,

$$2\sigma^+ = \rho_{11} + \rho_{1-1}$$

and

$$2\sigma^- = \rho_{11} - \rho_{1-1},$$

represent the fractions of natural parity $[P = (-1)^J]$ and unnatural parity $[P = -(-1)^J]$ exchange in the production mechanism, respectively. Figures 35 and 36 show σ^+ and σ^- as a function of t for the $\overline{K}^{*0}(890)$ and the $K^{*-}(890)$, respectively. Again, the s-wave background effects are ignored in calculating σ^+ and σ^-.

For the $\overline{K}^{*0}(890)$ where only isovector exchange is allowed, both σ^+ and σ^- in Fig. 35 rise sharply

TABLE X. Density-matrix elements for the $K^{*-}(890)$ evaluated in the Jackson frame.

$\|t\|$ Range (GeV^2)	Events[a] $d\sigma/dt$	Jackson frame ρ_{00}	ρ_{11}	$Re\rho_{10}$	ρ_{1-1}
0.003–0.05	78 (873 ± 99)	0.327 ± 0.081	0.337 ± 0.040	−0.127 ± 0.049	0.161 ± 0.070
0.05 –0.10	133 (1030 ± 90)	0.180 ± 0.058	0.410 ± 0.029	−0.076 ± 0.029	0.289 ± 0.050
0.10 –0.20	253 (980 ± 62)	0.117 ± 0.040	0.442 ± 0.020	−0.082 ± 0.022	0.350 ± 0.037
0.20 –0.30	159 (616 ± 49)	0.059 ± 0.048	0.470 ± 0.024	−0.014 ± 0.028	0.365 ± 0.046
0.30 –0.50	143 (277 ± 23)	0.094 ± 0.053	0.453 ± 0.027	−0.013 ± 0.031	0.345 ± 0.053
0.50 –0.75	54 (83 ± 11)	0.035 ± 0.083	0.483 ± 0.041	−0.027 ± 0.041	0.467 ± 0.080
0.75 –1.00	29 (44.9 ± 8.3)	−0.055 ± 0.100	0.528 ± 0.050	−0.134 ± 0.066	0.106 ± 0.129
1.00 –1.50	36 (27.9 ± 4.6)	0.107 ± 0.090	0.446 ± 0.045	0.074 ± 0.070	0.305 ± 0.106

[a]In units of $\mu b/GeV^2$.

from $t=0$ and stay, respectively, at about 0.6 and 0.2 in the large-t region. The nonzero value of σ^- suggests that unnatural-parity vector exchange, such as B, is important. However, it should be noted that pion exchange can also give a nonzero value of σ^- if absorptive effects (Regge cuts) are taken into account. For the $K^{*-}(890)$, where both isoscalar and vector exchanges are allowed, Fig. 36 shows σ^+ rising sharply from $t=0$ and remaining at about 0.8 in the large-t region. In contrast to σ^- for the $\overline{K}^{*0}(890)$, σ^- for the $K^{*-}(890)$ is essentially zero out to large $|t|$ values. This suggests that the unnatural-parity exchanges are less important for $\overline{K}^{*-}(890)$ than for $\overline{K}^{*0}(890)$ production. We note that the $I=1$ exchange amplitude for $K^{*-}(890)$ production is smaller by a factor of 2 than that for $\overline{K}^{*0}(890)$.

VI. The $K^*(1420)$

It has generally been accepted that a single $J^P = 2^+$ $K\pi$ state exists with $K\pi$ mass centered at 1.42 GeV. Recent work[27] on the reaction

$$K^+d \to K^+\pi^- pp_s \tag{6.1}$$

suggests that there is, in addition, an s-wave $K\pi$ enhancement at 1.36 GeV. This state, if it exists, gives rise to an additional background problem and complicates the analysis of the $K^*(1420)$ production and decay properties. Further discussion of this state will be deferred until Sec. VII. In the present section, we assume that all events in the mass band defined below belong to a single resonance, the $K^*(1420)$.

A. Production of the $K^*(1420)$

The charged and neutral $K^*(1420)$ are produced in the reactions

$$K^-p \to K^{*-}(1420)p \quad (\searrow K^-\pi^0 + \overline{K}^0\pi^-), \tag{6.2}$$

$$K^-p \to \overline{K}^{*0}(1420) \quad (\searrow K^-\pi^+). \tag{6.3}$$

Again, in studying the $K^{*-}(1420)$, data from both

TABLE XI. Density-matrix elements for the $K^{*-}(890)$ evaluated in the helicity frame.

$\|t\|$ Range (GeV^2)	No. of events	Helicity frame ρ_{00}	ρ_{11}	$Re\rho_{10}$	ρ_{1-1}
0.003–0.05	78	0.451 ± 0.088	0.275 ± 0.044	0.010 ± 0.043	0.223 ± 0.070
0.05 –0.10	133	0.252 ± 0.059	0.374 ± 0.030	−0.030 ± 0.032	0.325 ± 0.053
0.10 –0.20	253	0.196 ± 0.043	0.402 ± 0.021	−0.048 ± 0.021	0.390 ± 0.035
0.20 –0.30	159	0.110 ± 0.048	0.445 ± 0.024	−0.001 ± 0.028	0.391 ± 0.047
0.30 –0.50	143	0.107 ± 0.052	0.447 ± 0.026	−0.008 ± 0.031	0.351 ± 0.053
0.50 –0.75	54	−0.001 ± 0.080	0.500 ± 0.040	−0.035 ± 0.040	0.449 ± 0.082
0.75 –1.00	29	0.284 ± 0.135	0.358 ± 0.067	−0.200 ± 0.057	0.276 ± 0.113
1.00 –1.50	36	0.223 ± 0.121	0.388 ± 0.060	0.034 ± 0.057	0.363 ± 0.100

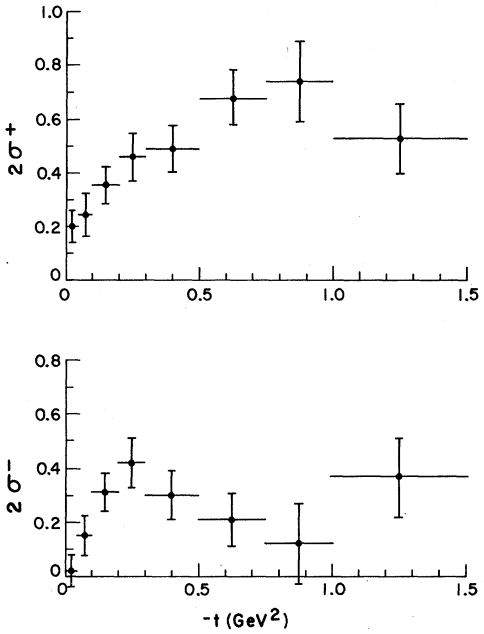

FIG. 35. σ^+ and σ^- evaluated in the helicity frame for the $\overline{K}^{*0}(890)$.

charge states $K^-\pi^0$ and $K^0\pi^-$ were combined. The $K^*(1420)$ mass interval is taken as $1.30 < M(K^*(1420)) < 1.50$ GeV for all reactions. Figures 37(a) and 38(a) show the momentum-transfer-squared distributions for reactions (6.2) and (6.3), respectively. As seen in Figs. 27–29, substantial backgrounds exist underneath the $K^*(1420)$ signals

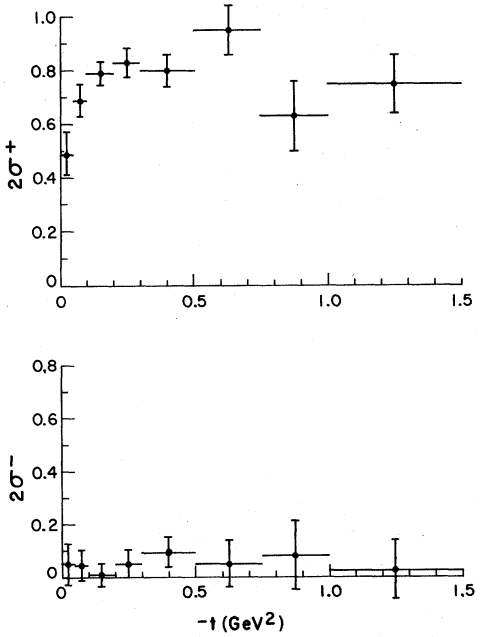

FIG. 36. σ^+ and σ^- evaluated in the helicity frame for the $K^{*-}(890)$.

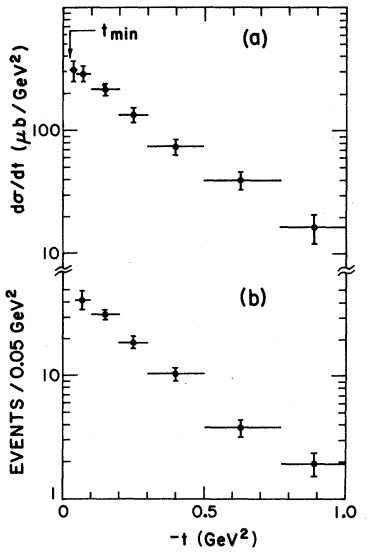

FIG. 37. (a) Differential cross section for reaction (6.2) and (b) dN/dt for the events in the control region.

for all reactions. We also show the momentum-transfer distribution for the background events defined by mass cuts:

$$1.20 < M(K\pi) < 1.30 \text{ GeV},$$

$$1.50 < M(K\pi) < 1.60 \text{ GeV}$$

in Figs. 37(b) and 38(b). We note that both events in the signal region and in the control region show similar behavior of the t-distributions. The slope of $d\sigma/dt$ is steeper for the neutral $K^*(1420)$ than that for the charged $\overline{K}^*(1420)$. In both cases, we parametrize $d\sigma/dt$ with an exponential form in t,

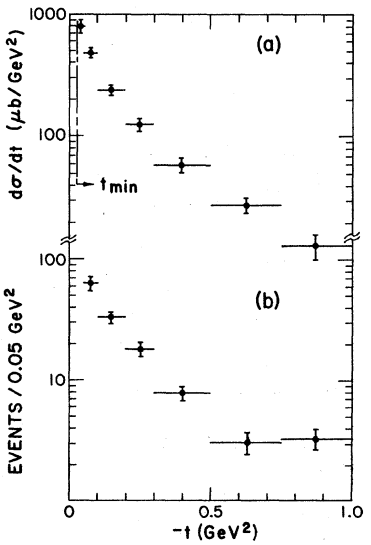

FIG. 38. (a) Differential cross section for reaction (6.3) and (b) dN/dt for the events in the control region.

$d\sigma/dt = Ae^{Bt}$, for $0.031 < t < 0.5$ GeV^2. We find that

$B = 4.1 \pm 1.2$ GeV^{-2} for reaction (6.2),

$B = 7.3 \pm 1.2$ GeV^{-2} for reaction (6.3)

for the signal region and

$B = 5.7 \pm 1.4$ GeV^{-2} for reaction (6.2),

$B = 6.2 \pm 1.4$ GeV^{-2} for reaction (6.3)

for the control region. These results seem to indicate a significant difference in the production mechanism of the charged and the neutral $K^*(1420)$.

B. Decay of the $K^*(1420)$

As discussed in Sec. VIA, substantial background exists in the $K^*(1420)$ mass region for all reactions, and the decay angular distribution of the $K^*(1420)$ can be strongly influenced by the background. The control regions of the $K^*(1420)$ may be expected to provide some information regarding the background amplitude, but because of the statistical limitations of our data and the rapid change in the decay angular distribution as a function of $K\pi$ mass, as seen in Sec. VII, it is not possible to obtain the background amplitude reliably. Thus, we will show the density-matrix elements assuming only the D-wave amplitude and ignoring the background wave.

Figures 39 and 40 show the density-matrix elements for reactions (6.2) and (6.3), respectively, as a function of t. The density-matrix elements are obtained from the $\langle Y_l^m \rangle$ moments of the decay angular distribution using the relations

$$\rho_{2-2} = 7(4\pi/70)^{1/2}\langle Y_4^4 \rangle,$$

$$\mathrm{Re}\rho_{2-1} = -\tfrac{7}{2}(4\pi/35)^{1/2}\langle Y_4^3 \rangle,$$

$$\rho_{1-1} = -(4\pi/10)^{1/2}[2\langle Y_4^2 \rangle + \sqrt{3}\,\langle Y_2^2 \rangle],$$

$$\mathrm{Re}\rho_{2\,0} = (4\pi/20)^{1/2}[\sqrt{3}\,\langle Y_4^2 \rangle - 2\langle Y_2^2 \rangle],$$

$$\mathrm{Re}\rho_{1\,0} = \tfrac{1}{2}(4\pi/10)^{1/2}[\sqrt{2}\,\langle Y_2^1 \rangle + 2\sqrt{3}\,\langle Y_4^1 \rangle],$$

$$\mathrm{Re}\rho_{2\,1} = (4\pi/10)^{1/2}[\sqrt{3}\,\langle Y_2^1 \rangle - \tfrac{1}{2}\sqrt{2}\,\langle Y_4^1 \rangle],$$

$$\rho_{1\,1} = \tfrac{1}{5}\sqrt{4\pi}\,[\tfrac{1}{2}\sqrt{5}\,\langle Y_2^0 \rangle - 2\langle Y_4^0 \rangle] + \tfrac{1}{5},$$

$$\rho_{0\,0} = \tfrac{1}{5}\sqrt{4\pi}\,[\sqrt{5}\,\langle Y_2^0 \rangle + 3\langle Y_4^0 \rangle] + \tfrac{1}{5},$$

with the normalization condition

$$\rho_{00} + 2\rho_{11} + 2\rho_{22} = 1.$$

The errors in Figs. 39 and 40 are statistical only and contain no contribution for background uncertainties. One notes that, for $|t|$ smaller than 0.4 GeV^2, the values of ρ_{22} are unphysical by about 2 standard deviations, presumably due to interference between the resonant and background waves. In general, the elements ρ_{ij} show rather similar dependences on t for both $K^*(1420)$. The interpretation of ρ_{00} and ρ_{11} at small t is complicated by the

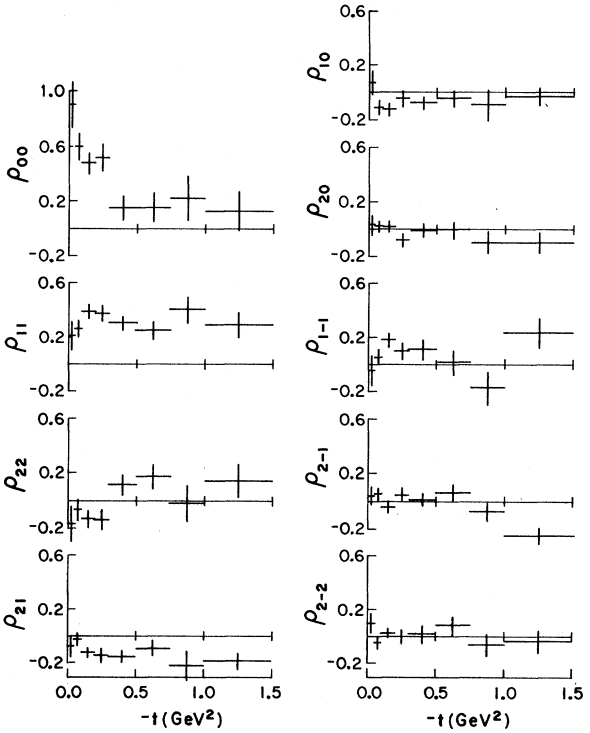

FIG. 39. $K^{*-}(1420)$ density-matrix elements, evaluated in the Jackson frame, as a function of t.

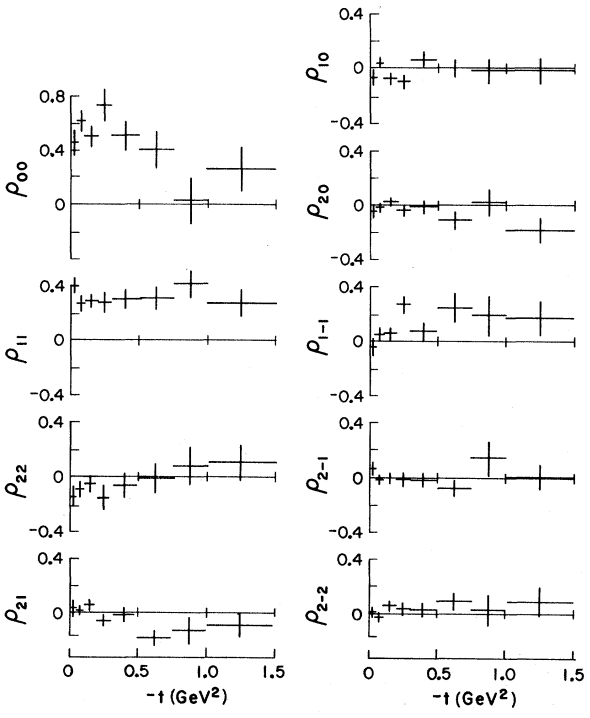

FIG. 40. $\bar{K}^*(1420)$ density-matrix elements, evaluated in the Jackson frame, as a function of t.

previously noted unphysical value of ρ_{22}, however, one sees that ρ_{00} falls off more rapidly as a function of t for the charged $K^*(1420)$. An OPE calculation[28] for the 2^+-meson production in the reaction $0^- + N \to N + 2^+$ predicts $\rho_{00} = 1$ and all others = 0 for pseudoscalar-meson exchange and $\rho_{11} = 0.5$, $\rho_{1-1} \to 0.5$ $(t \to 0)$ and all others = 0 for vector-meson exchange. Thus, the observed large value of ρ_{00} for both reactions indicates a substantial π-exchange contribution for $\bar{K}^{*0}(1420)$ and $K^{*-}(1420)$ production. The nonzero values of ρ_{11} and ρ_{1-1} suggest that some vector-meson-exchange contribution is required for both charged- and neutral-$K^*(1420)$ production.

VII. THE $K\pi$ SYSTEM

Careful study of the $K\pi$ invariant-mass distributions in Figs. 27 and 28 reveals no significant effects additional to those already discussed for $(K\pi)^-$. However, in the case of $(K\pi)^0$, Fig. 29, one notes the small dip in the mass distribution following the sharp fall from the $\bar{K}^{*0}(1420)$ peak and the shoulder appearing on the low side of this peak.[29] Recent results for reaction (6.1) have suggested the existence of two further $K\pi$ states at 1.36 GeV (Ref. 27) and 1.8 GeV.[30] The latter effect could account for the appearance of the above-mentioned dip in the $K^-\pi^+$ mass distribution. There have been further suggestions of $K\pi$ states at masses 1.10 GeV (Ref. 31) and 1.26 GeV (Ref. 32) which do not appear in the present data.

Additional information on the $K\pi$ system is obtained from the spherical harmonic moments, $\langle Y_l^m \rangle$, of the $K\pi$ angular distribution. In Figs. 41–43, we show the $m = 0$ moments for $l \leq 8$, evaluated in the Jackson frame, for reactions (1.2) to (1.4), respectively. The survey is restricted to $|t| < 1.0$ GeV^2, and it covers the $K\pi$ mass range 0.7–2.1 GeV. The $\langle Y_l^0 \rangle$ for reactions (1.2) and (1.3) are displayed separately since any interference effects

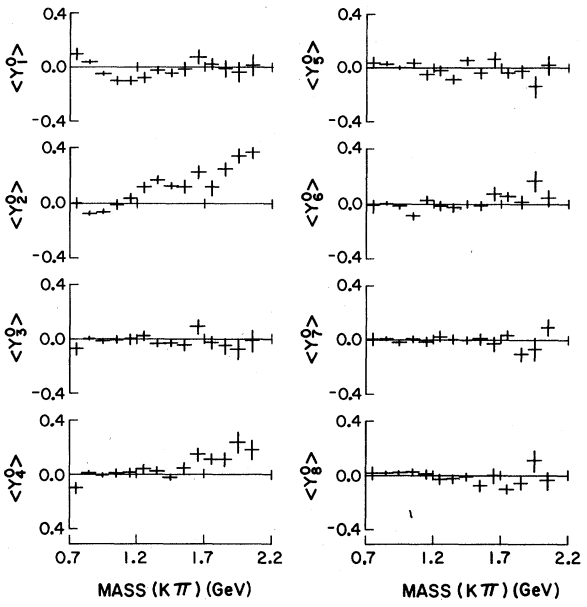

FIG. 42. $\langle Y_l^0 \rangle$ moments as a function of $K\pi$ mass for reaction (1.3).

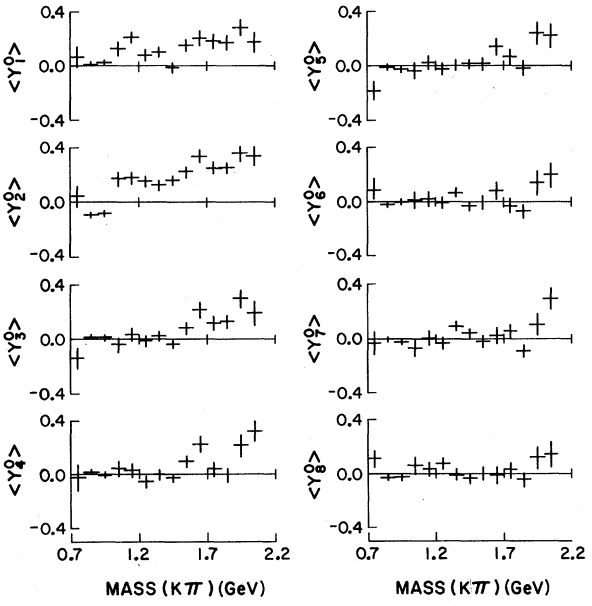

FIG. 41. $\langle Y_l^0 \rangle$ moments as a function of $K\pi$ mass for reaction (1.2).

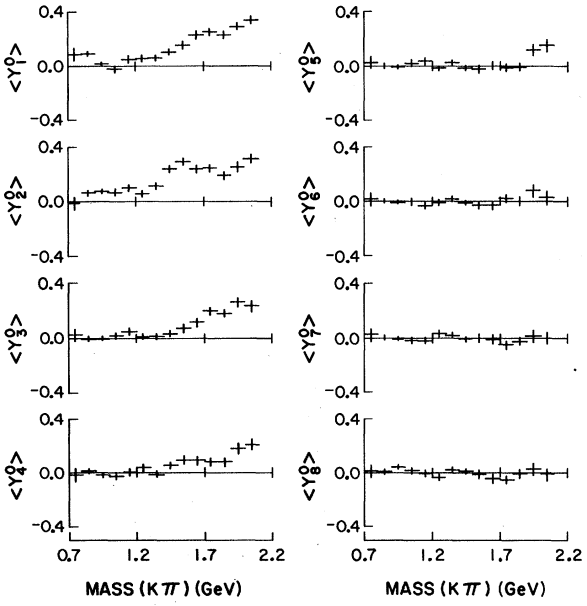

FIG. 43. $\langle Y_l^0 \rangle$ moments as a function of $K\pi$ mass for reaction (1.4).

between the $I=\frac{1}{2}$ and $I=\frac{3}{2}$ $K\pi$ states would differ for the $\bar{K}^0\pi^-$ and $K^-\pi^0$ states. For $l \geq 5$, the $\langle Y_l^0 \rangle$ for all three reactions show essentially zero values for $K\pi$ mass below 1.9 GeV. Above 1.9 GeV, all $\langle Y_l^0 \rangle$ with $l \geq 5$ for (1.2) and $\langle Y_5^0 \rangle$ for (1.4) become significant, whereas for (1.3), all $\langle Y_l^0 \rangle$ with $l \geq 5$ remain essentially zero. This could be related to the presence of the diffractive $K\pi$ scattering, which can occur in reactions (1.2) and (1.4), but not in reaction (1.3). This interpretation is consistent with the small values of $\langle Y_1^0 \rangle$ and $\langle Y_3^0 \rangle$ in this mass range for reaction (1.3) compared to the much larger values for (1.2) and (1.4). From these figures, we note that the $\langle Y_l^0 \rangle$ moments show no significant effects associated with the proposed enhancements at 1.36 GeV and 1.8 GeV.

Now, we discuss in more detail the s-wave $K\pi$ effect at 1.36 GeV which has been suggested by a study[27] of the angular correlations of the $K^+\pi^-$ system in reaction (6.1). This state was isolated from the $K^*(1420)$ by imposing the restriction $|\cos\theta|<0.7$ on the Jackson angle of the $K\pi$ system. Since both reactions (6.1) and (1.4) produce the neutral $K\pi$ system in association with nucleon charge exchange, they are expected to exhibit rather similar characteristics. In Figs. 44(a) and (b), we show, respectively, the $K^-\pi^+$ mass distributions from reaction (1.4) for events with $|\cos\theta| > 0.7$ and with $|\cos\theta|<0.7$. In Fig. 44(b), we observe a peak at about 1.36 GeV, supporting the previous suggestion of a $K\pi$ enhancement at this mass. However, we note that interference between a smooth s-wave and the resonant d-wave amplitude [$K^*(1420)$] can produce a mass shift of 50 MeV for the $K^*(1420)$ if such a cut is made.[33] For comparison, we have made the same analysis for the non-charge-exchange reactions (1.2) and (1.3). No significant effect is observed.

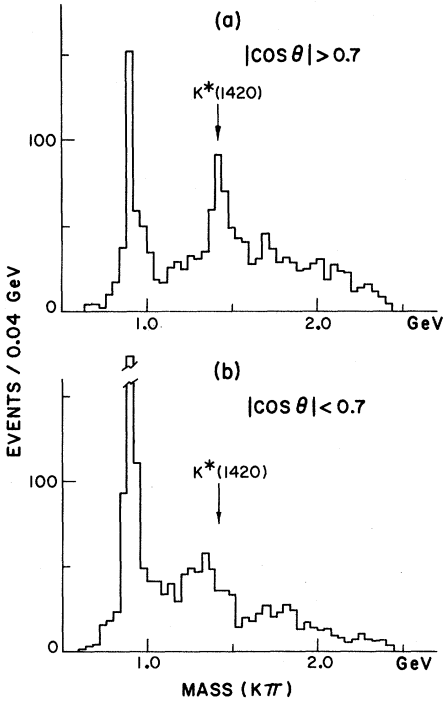

FIG. 44. The $K^-\pi^+$ mass distributions for (a) $|\cos\theta| > 0.7$, (b) $|\cos\theta| < 0.7$.

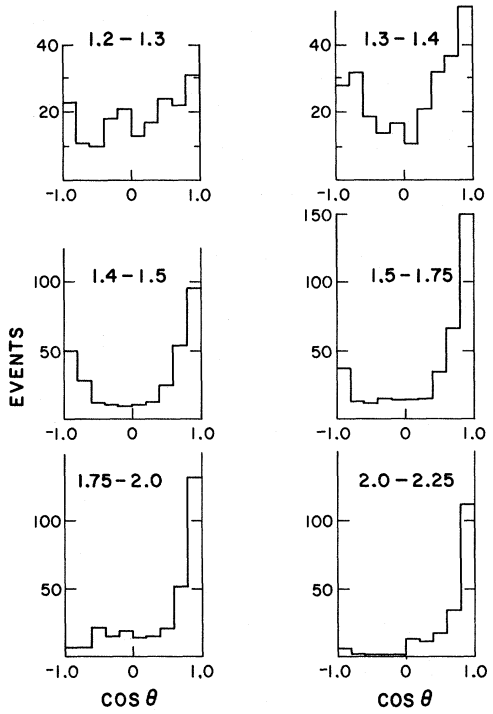

FIG. 45. Decay angular distributions for reaction (1.4) for the $K\pi$ mass intervals given in the figure.

Finally, we discuss in more detail the recently

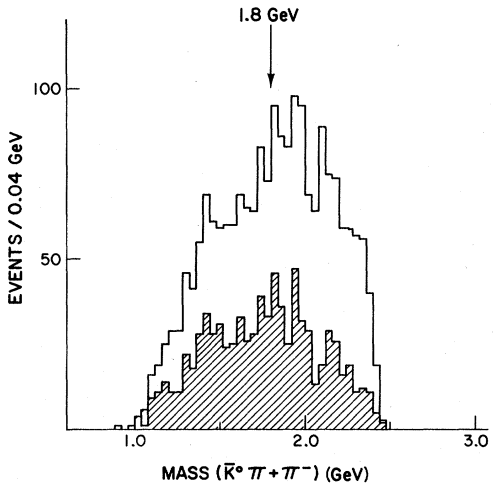

FIG. 46. $\bar{K}^0\pi^+\pi^-$ mass distribution. The shaded area corresponds to events with $t' < 0.25$ GeV^2.

TABLE XII. Parametrization of the Regge-pole trajectories used in the B_5 calculation.

$$\alpha(X)=\alpha_0+\delta+\alpha' X$$

Trajectory	α_0	δ	α'
$\omega - A_2$	0.48	0	0.9
Δ	0.13	$\frac{1}{2}$	0.9

$$\alpha(X)=(\alpha_0+\alpha' X)+ia(X-X_0)$$

Trajectory	α_0	α'	a	X_0
N	−0.37	1	0.14	1.0
Λ	−0.68	0.95	0.14	2.1

$$\alpha(X)=\theta(X_{\mathrm{Th}}-X)(\alpha_0+\alpha'_- -X)$$
$$+\theta(X-X_{\mathrm{Th}})[(\alpha_0+\alpha'_+ +X)+ia(X-X_0)]$$

Trajectory	α_0	α'_-	α'_+	a	X_0	X_{Th}
K^*	0.35	0.9	0.82	0.07	0.29	0.406

proposed $J^P=3^-$ $K\pi$ state around 1.8 GeV.[30] We refer to the scatter plot of $\cos\theta$ for the Jackson frame against the $K\pi$ invariant mass, Fig. 26, where a clear concentration of events appears with $\cos\theta \sim 0.3$ and mass ~1.8 GeV. In Fig. 45, we select from this plot the $K\pi$ angular distribution for reaction (1.4) for several intervals in the $K\pi$ mass between 1.2 GeV and 2.25 GeV. The distributions for $K\pi$ mass between 1.5 GeV and 2.25 GeV are very similar to those already reported for reaction (6.1). Note also that the angular distributions vary quite rapidly as a function of mass. It has also been suggested[30] that the proposed state decays into $K\pi\pi$ in addition to $K\pi$. For completeness, we show in Fig. 46 the $K\pi\pi$ invariant mass from the reaction

$$K^-p \to \bar{K}^0\pi^-\pi^+n$$

taken from Ref. 1. The shaded area corresponds to events with $|t'|<0.25$ GeV^2. This distribution does not show a statistically meaningful enhancement at about 1.8 GeV, unlike the previous observation.[30] Although the results presented here suggest that the effects observed around 1.8 GeV for reaction (6.1) also appear for reaction (1.4), the statistical level of the data precludes definite confirmation of the effect.

VIII. THE $K^0\pi^-p$ FINAL STATE; B_5 SCHEMES

Models based on an extension of the dual-Regge model[34] to five external particles have been proposed[35] and compared[36] with previous data. These schemes, known generically as B_5, construct what purports to be the physical scattering amplitude for that class of reactions which are dominated by

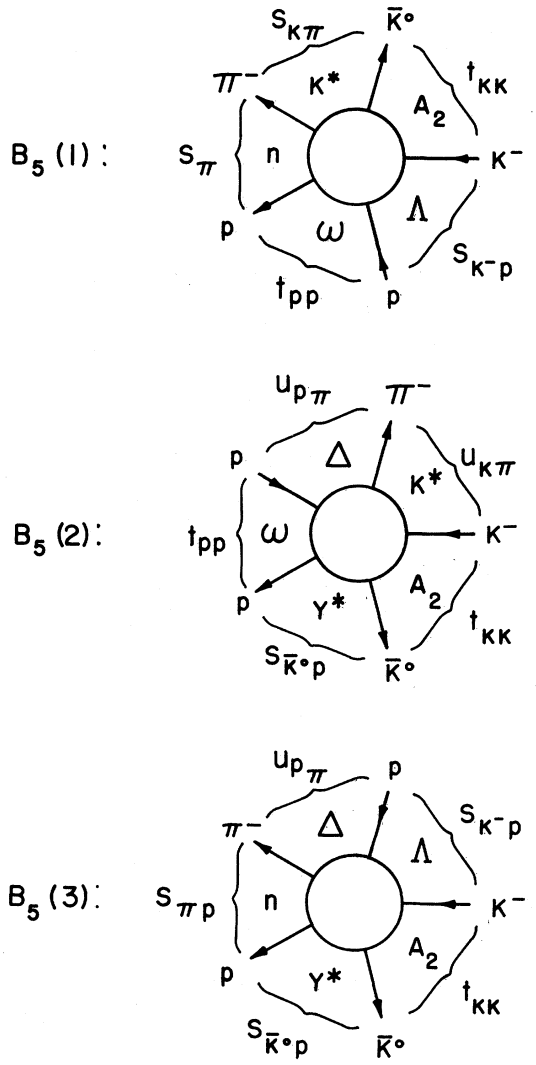

FIG. 47. The five-point diagrams with associated Regge trajectories and kinematic variables used in the calculation of B_5.

vector-meson exchange and which have no Pomeranchon contribution; the reaction $K^-p \to \bar{K}^0\pi^-p$ falls into this class. With this amplitude it is possible to predict all possible spectra and give their energy dependence. The good qualitative success of the B_5 schemes for many distributions then leads us to compare some of the more detailed behavior of these predicted spectra to our data.

The particular amplitude we have chosen to work with is that used by Chan Hong-Mo *et al.*[37] This model has an amplitude given by[38]

$$M = A \times F_{\mathrm{Kin}}(P_{K^-},\ P_p,\ P_{\bar{K}^0},\ P_{\pi^-})$$
$$\times[B_5(1)+B_5(2)+B_5(3)],$$

where

$B_5(1) = B_5(1-\alpha_{K^*},\ 1-\alpha_A,\ 1-\alpha_\Lambda,\ 1-\alpha_\omega,\ \frac{1}{2}-\alpha_N)$,

$B_5(2) = B_5(1-\alpha_{K^*},\ 1-\alpha_A,\ \frac{3}{2}-\alpha_{Y^*},\ 1-\alpha_\omega,\ \frac{3}{2}-\alpha_\Delta)$,

$B_5(3) = B_5(\frac{3}{2}-\alpha_\Delta,\ \frac{1}{2}-\alpha_\Lambda,\ 1-\alpha_A,\ \frac{3}{2}-\alpha_{Y^*},\ \frac{1}{2}-\alpha_N)$,

and

$$F_{\rm Kin} = \epsilon_{\alpha\beta\gamma\delta} P_K^{\alpha} P_p^{\beta} P_{\bar{K}}^{\gamma} P_\pi^{\delta},$$

is a kinematical factor approximating the effects of the spin of the external baryons. $B_5(X_1, X_2, X_3, X_4, X_5)$ is the Bardakci-Ruegg[35] five-point function defined by

$$B_5(X_1,X_2,X_3,X_4,X_5) = \int_0^1\int_0^1\int_0^1\int_0^1 du_1\,du_2\,du_4\,du_5\,\delta(u_1+u_2-1)\,\delta(u_5+u_4-1)\,u_1^{X_1-1}u_2^{X_2-1}(1-u_2u_4)^{X_3-X_1-X_5} \times u_4^{X_4-1}u_5^{X_5-1}$$

and $\epsilon_{\alpha\beta\gamma\delta}$ is the totally antisymmetric tensor in four variables ($\epsilon_{0123}=+1$). The different α's are the Regge-pole trajectories and their parametrization is given in Table XII. The kinematic variables for each trajectory are illustrated in Fig. 47. The final spectra were obtained using a Monte Carlo technique[39] to generate approximately 170 000 events. By normalizing the predictions of the model to our total number of events, we are able to fix the single adjustable parameter, A.

Figures 48(a), 48(b), and 48(c) show the effective mass distributions of the $(\bar{K}^0\pi^-)$, (K^0p), and (π^-p) systems, respectively. The amounts of $K^*(890)$ and $K^*(1420)$ predicted are both somewhat higher than the data.[40] Little structure is seen in the $(\bar{K}^0p)$ mass distribution and the theoretical curve is in substantial agreement with the data here.[41] The π^-p mass distribution, however, is not adequately described by B_5. The predicted but unobserved low-mass peak occurring at 1.35 GeV

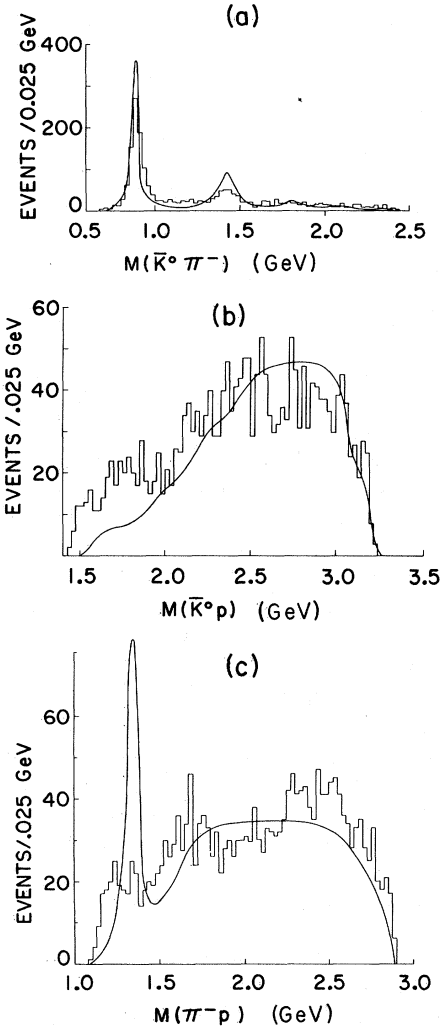

FIG. 48. (a) $\bar{K}^0\pi^-$ mass spectrum, (b) $\bar{K}^0p$ mass spectrum, (c) π^-p mass spectrum. The curves are the spectra as predicted by B_5 and normalized to the total number of events in the channel $K^-p \to \bar{K}^0\pi^-p$.

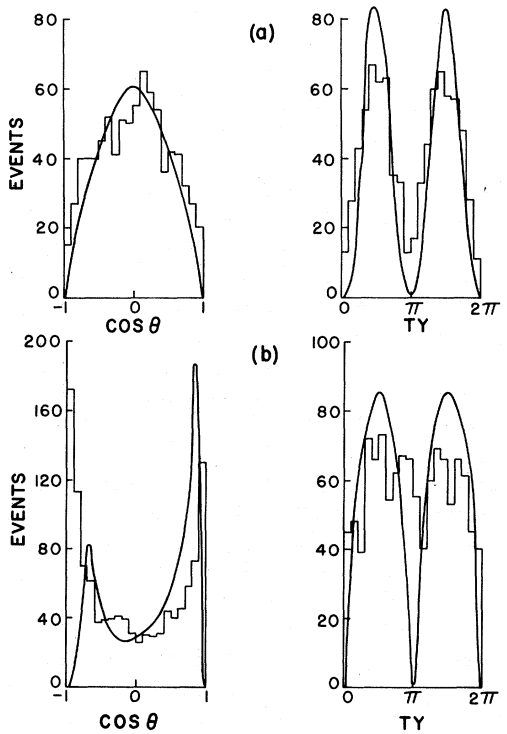

FIG. 49. The decay angular distributions for the events with $K\pi$ mass (a) in the interval 0.825–0.975 GeV and (b) less than 1.0 GeV. The curves are the B_5 predictions.

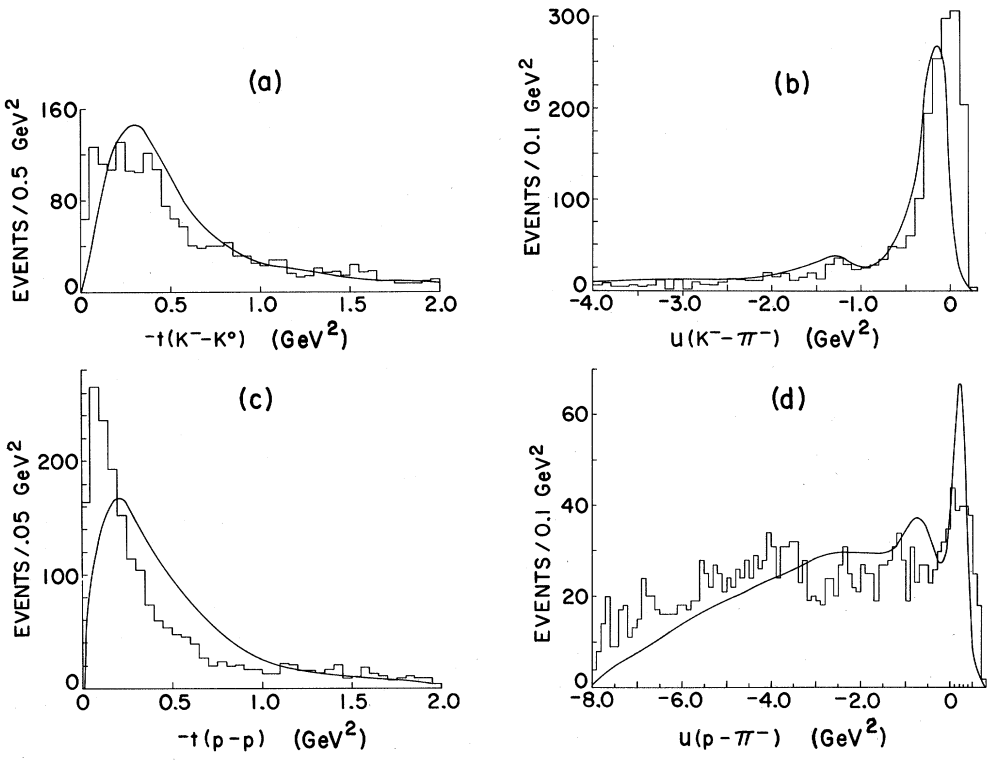

FIG. 50. Four-momentum-transfer-squared distributions for (a) K^- to $\overline{K}^0(t_{KK})$, (b) K^- to $\pi^-(u_{K\pi})$, (c) incident p to outgoing $p\,(t_{pp})$, (d) incident p to $\pi^-(u_{p\pi})$; all with B_5 curves.

is associated with the daughter of the first recurrence of the nucleon and not with the $\Delta(1236)$.

We utilize the Gottfried-Jackson frame for the $\overline{K}^0\pi^-$ system and show the angular distributions of the $\overline{K}^0$ in Fig. 49 (Ref. 42) for the $K^0\pi^-$ mass interval 0.825–0.975 GeV and also for mass > 1.0 GeV. The change in the polar angle distribution from approximately $\sin^2\theta$ to dominantly $\cos^2\theta$ is correctly given by this model. For the region above 1.0 GeV, the predicted forward-backward asymmetry is opposite to that given by the data, and the predicted zeros in the Treiman-Yang angular distribution are not observed. These zeros are a consequence of the simple kinematical factor used in front of the amplitude. It appears necessary to be able to treat external particles with spin in a better way. In addition, there is the possibility that inclusion of some pion exchange and/or allowance for absorption effects is necessary to fully describe these distributions.

Figures 50(a), 50(b), 50(c), and 50(d) show the four-momentum-transfer-squared distributions for K^- to $\overline{K}^0$ (t_{KK}), K^- to π^- $(u_{K\pi})$, incoming p to outgoing p (t_{pp}), and incoming p to π^- $(u_{p\pi})$, respectively. Although the data seem to be fairly well described for the t_{KK} and $u_{K\pi}$ distributions (the t_{KK} distribution is slightly more forward-peaked while the $u_{K\pi}$ distribution is slightly sharper and more backward-peaked than predicted by B_5), the theory has much more trouble in describing the proton four-momentum distributions. The t_{pp} spectrum is more forward-peaked and considerably sharper than suggested by the model[43] while the strong "dip-bump" structure[44] in the $u_{p\pi}$ distribution is not observed in the relatively flat experimental distribution.

Although many qualitative features are generally correct, certain distributions associated with the nucleon $[M(\pi^-p),\ u_{p\pi},\ t_{pp}]$ point out difficulties with the present B_5 calculations. Most of these problems may be traced to the difficulty in treating baryon spin correctly in the model.

ACKNOWLEDGMENTS

We wish to thank the personnel of the ANL and Chicago bubble-chamber scanning facilities for scanning and measuring. We would also like to acknowledge Dr. M. Derrick, Dr. E. Berger, and Dr. G. Fox for informative comments on this work. Thanks are also due to Miss S. Klepec for her very efficient typing.

*Work supported by the U. S. Atomic Energy Commission and in part by the National Science Foundation under University of Chicago Grant No. NSF GP-24126.

†Paper submitted by Herbert Schulz to the Department of Physics, the University of Chicago, in partial fulfillment of the requirement of the Ph.D. degree.

[1]F. Schweingruber, M. Derrick, T. Fields, D. Griffiths, L. G. Hyman, R. J. Jabbur, J. Loken, R. Ammar, R. E. P. Davis, W. Kropac, and J. Mott, Phys. Rev. 166, 1317 (1968).

[2]J. Mott, R. Ammar, R. Davis, W. Kropac, D. Slate, B. Werner, S. Dagan, M. Derrick, T. Fields, J. Loken, and F. Schweingruber, Phys. Rev. 177, 1966 (1969).

[3]W. W. M. Allison *et al.*, Nucl. Instr. Methods 84, 129 (1970).

[4]The results on elastic scattering from sample I are given in J. Mott, R. Ammar, R. Davis, W. Kropac, A. Cooper, M. Derrick, T. Fields, L. Hyman, J. Loken, F. Schweingruber, and J. Simpson, Phys. Letters 23, 171 (1966).

[5]D. Johnson, J. Loken, and T. Wangler, ANL POLLY Note No. 24, 1969 (unpublished).

[6]W. Galbraith *et al.*, Phys. Rev. 138, B913 (1965); W. F. Baker *et al.*, *ibid.* 129, 2285 (1963).

[7]This correction factor of 6% was obtained from a comparison with the sample of two-prong-plus-V events.

[8]J. Bärtsch *et al.*, CERN Report No. CERN-TH-70-51 (unpublished). This paper also notes that the small bump at $|t|=0.11$ GeV^2 is caused by the change from more accurate range measurements to the less accurate curvature measurements of the recoil proton momentum.

[9]C. Daum *et al.*, Nucl. Phys. B6, 273 (1965); A. Ashmore *et al.*, Phys. Rev. Letters 21, 387 (1968); Phys. Letters 28B, 61 (1968); K. J. Foley *et al.*, Phys. Rev. Letters 11, 503 (1963); 15, 45 (1965); V. Chabaud *et al.*, Phys. Letters 38B, 445 (1972).

[10]J. D. Jackson, Nuovo Cimento 34, 1644 (1964).

[11]We have also tried fourth- and sixth-order polynomial forms of PS(m). The results of all the fits are rather similar to each other.

[12]Particle Data Group, Rev. Mod. Phys. 43, S1 (1971).

[13]M. Aguilar-Benitez, R. L. Eisner, and J. B. Kinson, Phys. Rev. D 4, 2583 (1971).

[14]The form of PS(m) used for this study is PS(m) = $a(m - 0.63)$.

[15]E. L. Berger and G. C. Fox, Phys. Letters 36B, 389 (1971).

[16]C. Lovelace, in *Proceedings of a Conference on the $\pi\pi$ and $K\pi$ Interactions at Argonne National Laboratory, 1969,* edited by J. Loeffler and E. Malamud (Argonne National Laboratory, Argonne, Ill., 1969).

[17]H. R. Rubinstein, Phys. Rev. Letters 17, 41 (1966).

[18]K. Gottfried and J. D. Jackson, Nuovo Cimento 34, 735 (1964).

[19]J. T. Donohue, Phys. Rev. 163, 1549 (1967).

[20]G. V. Dass and C. D. Froggatt, Nucl. Phys. B10, 496 (1969).

[21]The helicity frame is defined in the $K^*(890)$ rest frame with z axis opposite to the direction of the recoil neutron and with y axis in the direction $\hat{y} = \vec{K}_{in}^{-} \times \vec{K}_{out}^{*} / |\vec{K}_{in}^{-} \times \vec{K}_{out}^{*}|$, where $\vec{K}_{in}^{-}$ and $\vec{K}_{out}^{*}$ are the momenta of the incident and outgoing K mesons, respectively.

[22]G. Fox *et al.*, Phys. Rev. D 4, 2647 (1971).

[23]D. D. Carmony *et al.*, Nucl. Phys. B12, 9 (1969). The pion- and vector-meson-exchange amplitudes interfere constructively for K^-p, as suggested in Ref. 19.

[24]Aachen-Berlin-CERN-London-Vienna Collaboration, CERN Report No. CERN-TH-71-24 (unpublished); Nucl. Phys. B5, 567 (1968).

[25]M. Markytan, Nucl. Phys. B10, 193 (1969).

[26]J. P. Ader *et al.*, Nuovo Cimento 56A, 952 (1968).

[27]A. Firestone *et al.*, Phys. Rev. Letters 26, 1460 (1971).

[28]H. Hogaasen *et al.*, Nuovo Cimento 42A, 323 (1966).

[29]As discussed in Sec. IV C, it was not possible to determine the width of the $\overline{K}^{*0}(1420)$ in the present experiment, due to the prominent shoulder appearing on the low side of the mass peak. This feature is not obvious in charged $K^*(1420)$ production.

[30]D. D. Carmony *et al.*, Phys. Rev. Letters 27, 1160 (1971); A. Firestone *et al.*, Phys. Letters 36B, 513 (1971).

[31]T. C. Trippe *et al.*, Phys. Letters 28B, 203 (1968).

[32]W. P. Dodd *et al.*, Phys. Rev. 177, 1991 (1969).

[33]In a simple model with a constant s wave, $s\exp(i\delta_0)$, and a resonant $K^*(1420)$ d wave, a value of $\delta_0 \approx 110°$, for example, will reproduce the observed mass shift of ~ 50 MeV with the cut $|\cos\theta| \leq 0.7$, although the ratio of s to d waves is then larger than experimentally observed.

[34]G. Veneziano, Nuovo Cimento 57A, 190 (1968).

[35]K. Bardakci and H. Ruegg, Phys. Letters 28B, 342 (1968); J. F. L. Hopkinson and E. Plahte, Phys. Letters 28B, 489 (1969).

[36]Chan Hong-Mo, CERN Report No. CERN-TH-1089 (unpublished); Chan Hong-Mo, R. O. Raitio, G. H. Thomas, and N. A. Tornquist, Nucl. Phys. B19, 173 (1970); J. Bärtsch *et al.*, *ibid.* B20, 63 (1970).

[37]Chan Hong-Mo, R. O. Raitio, G. H. Thomas, and N. A. Tornquist, Nucl. Phys. B19, 173 (1970).

[38]A fourth amplitude,

$$B_5(1-\alpha_{K^*}, \tfrac{1}{2}-\alpha_\Lambda, 1-\alpha_\omega, \tfrac{3}{2}-\alpha_{Y^*}, 1-\alpha_{K^*}),$$

is eliminated since it corresponds to a duality diagram which violates the rules of Harari and Rosner [H. Harari, Phys. Rev. Letters 20, 1395 (1968)].

[39]The Monte Carlo method used was based on that of J. H. Friedman, LRL Report No. UCRL-19206 (Rev.) (unpublished). The 170 000 events were obtained in two runs of 100 000 and 70 000 each and a weighted average taken of the spectra. The averaged weight and error for a given bin is

$$\bar{w} = (e_2^2 w_1 + e_1^2 w_2)/(e_1^2 + e_2^2), \qquad \bar{e} = e_1 e_2/(e_1^2 + e_2^2)^{1/2},$$

where w_1, w_2 and e_1, e_2 are the weights and errors for each of the points. The B_5 function was calculated using a program based on that devised by J. F. L. Hopkinson, Daresbury Nuclear Physics Lab. Report No. DNPL/P2 (unpublished).

[40]A still smaller peak visible at 1.8 GeV is a recurrence of the $K^*(890)$.

[41]The slightly bumpy structure of the B_5 curve is due to the recurrences of the Y_1^* at 1.8 and 2.2 GeV.

[42]We point out that these curves have not been renormalized to the data.

[43]The data show evidence for spin-nonflip coupling to the nucleon; the theory only has spin-flip coupling.

[44]The dip in the u distribution occurs because two of the three amplitudes are proportional to the factor $\alpha_\Delta + \frac{1}{2}$. Due to the choice by Chan Hong-Mo *et al.* of an intercept for α_Δ, this factor is zero at $u = -0.2$ (GeV/c)^2.